Journal of Computational and Applied Mechanics, Vol. 19, No. 1, (2024), pp. 37–79
DOI: 10.32973/jcam.2024.003

ANALYSIS OF OVERCORING IN SITU STRESS MEASUREMENT METHODS USING FINITE ELEMENT SIMULATIONS

Dávid Borza
Department of Energy Engineering, Faculty of Mechanical Engineering,
Budapest University of Technology and Economics
Műegyetem rkp. 3, 1111 Budapest, Hungary
borza.david@edu.bme.hu

Donát M. Takács
Department of Energy Engineering, Faculty of Mechanical Engineering,
Budapest University of Technology and Economics
Műegyetem rkp. 3, 1111 Budapest, Hungary
Montavid Thermodynamic Research Group
c/o ETTE, Lovas út 18., Budapest, 1012, Hungary
takacs@energia.bme.hu

[Received: March 20, 2024; Accepted: August 6, 2024]

Abstract. Two commonly used overcoring measurement methods for estimating the in situ stress state in rocks – the In Situ Stress Testing (IST) gauge and the Hollow Inclusion (HI) cell – are compared based on finite element models. The models simulate idealized measurement circumstances in homogeneous, isotropic and linearly elastic rocks during overcoring, and are used to evaluate the maximum accuracy achievable using the two methods. We show that while both methods are capable of accurately estimating the in situ stress state, their accuracy depends significantly on the placement of the instruments within the pilot hole. Recommendations regarding optimal instrument placement are given for both methods by considering stress disturbances created by the bore- and pilot holes.

1. Introduction

Estimation of the undisturbed underground or in situ stress state is essential to underground operations, such as mining, tunnelling and other geotechnical engineering projects. Since the in situ stress state is influenced by factors such as depth, tectonic forces, topography, constitutive behaviour of the rock, and the local geological history, among others [1], measurements are necessary to estimate the state of stress underground.

There are several techniques to determine the in situ stress state [2–4]. Hydraulic methods, such as hydraulic fracturing and the flat jack method, are based on pressure measurements. Their advantage is that these methods do not require knowledge of the material properties of the rock. On the other hand, they do not provide enough information to accurately estimate the entire three-dimensional in situ stress state, which can be necessary in certain cases. Methods based on displacement or strain measurements, such as overcoring, enable more accurate estimations. As the in situ stress state is derived from displacement or strain values, the constitutive behavior of the rock must be known. Typically, the rock is assumed to be linearly elastic. It is worth noting that there are methods that take the time dependence of the material behaviour into consideration, e.g., the Anelastic Strain Recovery (ASR) method [5, 6]. However, here, we work with the assumption of linear elasticity, as the unloading rate is assumed to be sufficiently low.

In the present paper we investigate two specific overcoring methods: the In situ Stress Testing (IST) method developed by Sigra, and the Hollow Inclusion (HI) cell developed by the Commonwealth Scientific and Industrial Research Organisation (CSIRO). Both methods use several assumptions in order to make calculations feasible, and best practice recommendations are given in order to confirm that the measurement circumstances conform to these assumptions and consequently the measurement results are accurate to some extent. Our goal is to independently verify such assumptions and recommendations and potentially improve them in order to ensure accurate measurement results.

The outline of the paper is as follows. First, we give an overview of overcoring methods in Section 2. This is followed by the exposition of the theory behind the IST and CSIRO HI measurement methods in Section 3, which is crucial for understanding the assumptions made during the evaluation of such measurements as well as for clearly showing the limitations of these methods. In Section 4, we construct a series of finite element models for the quasi-static simulation of a case study in the overcoring measurement process for the IST and CSIRO HI methods. We evaluate the results of these case studies regarding the theoretically achievable maximum accuracy of the estimated in situ stress state. Finally, in Section 5, we compare and contrast the two measurement techniques and give recommendations regarding the placement of the specific overcoring measurement instruments inside the pilot hole.

2. A concise overview of overcoring methods

One of the most common in situ stress measurement techniques in the mining industry is overcoring, which has been used since the 1960s [4]. The in situ stress state can be estimated based on the deformations and strains measured while the core is relieved. Naturally, the constitutive equations are necessary for the calculation of the stress state, therefore the material properties of the rock have to be measured. This is usually performed after the overcoring measurement itself, in a laboratory setting.

An overcoring measurement consists of three main steps, which are shown in Figure 1.

- *Step 1*: Drilling to the depth of the in situ stress state measurement itself. This main hole is usually called the borehole.
- *Step 2*: From the bottom of the borehole, a smaller diameter hole, the *pilot hole*, is drilled. An instrument, or gauge, is mounted in the pilot hole, which measures the deformations and strains of the pilot hole. (The specifics of this instrument depend on the measurement method used.)

- *Step 3*: A concentric hole is drilled around the instrument in the pilot hole, i.e. it is cored over. The outer diameter of this hole is identical or similar to the borehole diameter, and the inner diameter is larger than the pilot hole diameter. During this step, the remaining rock core is largely relieved from the in situ stress state, while the instrument installed in the pilot hole measures and records the deformations or strains throughout the process.

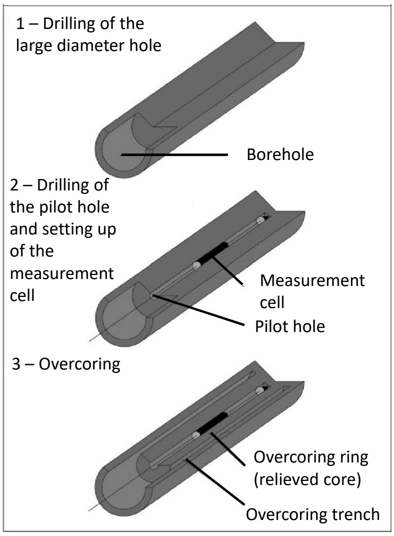

Figure 1. Steps of overcoring [7]

There are two main types of measurement tools that can be installed in the pilot hole. One of these measures the changes in diameter of the pilot hole during Step 3 by pins placed at different depths and orientations. The USBM (US Bureau of Mines) developed a gauge which measures the diameter change in three different orientations [8]. This provides enough data to estimate the in situ stress state in the plane perpendicular to the borehole axis with acceptable accuracy. Naturally, additional measurement data decreases the amount of total measurement error and the probability of instrument failure, therefore there are gauges that measure the pilot hole diameter during overcoring at multiple depths and orientations. For example, the IST gauge developed by SIGRA measures the diameter change in six different orientations [9]. The advantage of these instruments is that they can be used more than once, and there is no need for any cables during the measurements. The disadvantage of these gauges is that the in situ stress components parallel to the borehole axis cannot be estimated if the data is collected from a single hole [10]. Besides, this method is suitable only for relatively shallow depths. [2]

The other main type of overcoring instruments measures the strains of the pilot hole surface in different directions during Step 3. For example, the Hollow Inclusion

(HI) cell developed by CSIRO (Commonwealth Scientific and Industrial Research Organization) contains 9 or 12 strain gauges installed in different positions and orientations [11]. The advantage of these tools is that the full, three-dimensional in situ stress state can be estimated based on the data collected from a single hole. However, the CSIRO HI cell is glued into the pilot hole, so the cell can only be used once. A further disadvantage is that the epoxy-based glues cannot be applied in humid and dusty environments, and the thickness of the glue may influence the accuracy of the measurement [2].

A significant limitation of the overcoring technique is that the material properties of the rock must be known, since the in situ stress state is derived from deformation or strain values. Young's modulus and Poisson's ratio – and other parameters in case of anisotropic or nonlinear material behaviour – are usually determined by biaxial compression tests. These tests are usually carried out on the rock core remaining after Step 3 in the case of the CSIRO HI cell, and on nearby rock cores in the case of the IST method.

In the following section, the equations required to estimate the in situ stress state from the data collected by either an IST gauge or a CSIRO HI cell are presented.

3. Theoretical background of the evaluation of overcoring measurements

3.1. **Evaluation of IST measurements.** The IST gauge measures the change in diameter of the pilot hole during the relief of the rock core. The collected data can be used to determine the original in situ stress state, which still occurs sufficiently far (1.5–2.5 times the diameter of the borehole [11]) from the borehole.

3.1.1. *Assumptions.* In order to derive the in situ stress state from the changes in diameter of the pilot hole, the following assumptions are made:

- the stress state is identical in any plane perpendicular to the axis of the borehole,
- the drilling of the borehole and the pilot hole have no influence on the original in situ stress state,
- after overcoring, the rock core and the surface of the pilot hole are completely relieved from any stress,
- the rock is considered to be linearly elastic, homogeneous and isotropic,
- the axial in situ stress component is known. If the axis of the borehole is vertical, this component corresponds with the lithostatic (also called overburden) pressure, which is caused by the weight of the overlying material [4].

These assumptions imply that the deformations measured by the IST gauge are caused by the relief of the in situ stress state. As a consequence, a relationship must exist between the changes in diameter and the in situ stress state.

3.1.2. *Description of the stress state.* For describing the various stress states considered, the Cauchy stress tensor $\boldsymbol{\sigma}$ is used, which is assumed to be symmetric. We define a Cartesian coordinate system in which axis z coincides with the borehole axis. The components of this tensor are

$$\boldsymbol{\sigma} = \begin{bmatrix} \sigma_x & \tau_{xy} & \tau_{xz} \\ \tau_{xy} & \sigma_y & \tau_{yz} \\ \tau_{xz} & \tau_{yz} & \sigma_z \end{bmatrix}. \tag{3.1}$$

Accordingly, the change in the stress state near the pilot hole during Step 3 of overcoring is described by the (symmetric) tensor $\boldsymbol{\Delta\sigma}$ expressed as

$$\boldsymbol{\Delta\sigma} = \begin{bmatrix} \Delta\sigma_x & \Delta\tau_{xy} & \Delta\tau_{xz} \\ \Delta\tau_{xy} & \Delta\sigma_y & \Delta\tau_{yz} \\ \Delta\tau_{xz} & \Delta\tau_{yz} & \Delta\sigma_z \end{bmatrix}. \tag{3.2}$$

According to Section 3.1.1, the rock core is completely relieved after the overcoring, hence its loading changes:

$$\boldsymbol{\Delta\sigma} = \mathbf{0} - \boldsymbol{\sigma}^{\mathbf{0}}, \tag{3.3}$$

where $\boldsymbol{\sigma}^{\mathbf{0}}$ is the in situ stress state to be determined:

$$\boldsymbol{\sigma}^{\mathbf{0}} = \begin{bmatrix} \sigma_x^0 & \tau_{xy}^0 & \tau_{xz}^0 \\ \tau_{xy}^0 & \sigma_y^0 & \tau_{yz}^0 \\ \tau_{xz}^0 & \tau_{yz}^0 & \sigma_z^0 \end{bmatrix} = -\boldsymbol{\Delta\sigma}. \tag{3.4}$$

It is worth emphasizing here that these stress tensors describe the in situ stress state, which is the original, undisturbed stress state, and is different from the stress field close to the borehole. In most commonly used models, the in situ stress state is considered to be applied sufficiently far away from the borehole as a far-field boundary condition.

3.1.3. *Connection between stress state and deformations.* The change in diameter of the pilot hole Δd associated with the change in the loading of the core during the relief is given by [10]:

$$\begin{aligned} \Delta d = \frac{d}{E} \big[&(\Delta\sigma_x + \Delta\sigma_y) + 2(\Delta\sigma_x - \Delta\sigma_y)(1-\nu^2)\cos(2\theta) + \\ &+ 4\Delta\tau_{xy}(1-\nu^2)\sin(2\theta) - \nu\Delta\sigma_z \big], \end{aligned} \tag{3.5}$$

where d is the diameter of the pilot hole, E and ν are the Young's modulus and the Poisson's ratio of the rock, θ is the angle formed by the measured diameter and the x axis of the coordinate system. Note that this formula does not contain the τ_{xz} and τ_{yz} shear stress components, as the determination of these components would require measurements from boreholes with different orientations.

The IST gauge measures the changes in diameter in six different orientations (and depths) [9]. Using equations (3.4) and (3.5), the following can be written:

$$\begin{aligned} \Delta d_i = -\frac{d}{E} \big[&(\sigma_x^0 + \sigma_y^0) + 2(\sigma_x^0 - \sigma_y^0)(1-\nu^2)\cos(2\theta_i) + \\ &+ 4\tau_{xy}^0(1-\nu^2)\sin(2\theta_i) - \nu\sigma_z^0 \big], \quad i = 1, 2, \ldots, 6. \end{aligned} \tag{3.6}$$

This is a system of six linear equations. The variables are σ_x^0, σ_y^0, σ_z^0 and τ_{xy}^0, the components describing the in situ stress state. The system can be written in a matrix equation form as

$$\begin{pmatrix} \Delta d_1 \\ \vdots \\ \Delta d_6 \end{pmatrix} = \hat{\mathbf{A}} \begin{pmatrix} \sigma_x^0 \\ \sigma_y^0 \\ \sigma_z^0 \\ \tau_{xy}^0 \end{pmatrix}, \tag{3.7}$$

where:

$$\hat{\mathbf{A}} = -\frac{d}{E} \begin{pmatrix} 1+2(1-\nu^2)\cos(2\theta_1) & 1-2(1-\nu^2)\cos(2\theta_1) & -\nu & 4(1-\nu^2)\sin(2\theta_1) \\ \vdots & \vdots & \vdots & \vdots \\ 1+2(1-\nu^2)\cos(2\theta_6) & 1-2(1-\nu^2)\cos(2\theta_6) & -\nu & 4(1-\nu^2)\sin(2\theta_6) \end{pmatrix}. \tag{3.8}$$

Although the above system seems to be overdetermined at first glance, the equations are actually linearly dependent: it can be shown in a straightforward way that – assuming distinct θ_i – the rank of matrix $\hat{\mathbf{A}}$ is 3, i.e. it does not have full rank.

3.1.4. *Solution of the system.* In order to solve the (3.7) system of equations, σ_z^0 must be known to circumvent the linear dependence of the original equations. According to Subsection 3.1.1, we assume that it is entirely determined by the overburden pressure, which can be expressed as

$$\sigma_z^0 = -\rho g h, \tag{3.9}$$

where ρ is the mean density of the rocks above the location of the measurement, g is the gravitational acceleration, h is the depth measured from the surface.

Consequently, the system of equations (3.7) becomes

$$\underbrace{\begin{pmatrix} \Delta d_1 - \frac{d}{E}\nu\sigma_z^0 \\ \Delta d_2 - \frac{d}{E}\nu\sigma_z^0 \\ \Delta d_3 - \frac{d}{E}\nu\sigma_z^0 \\ \Delta d_4 - \frac{d}{E}\nu\sigma_z^0 \\ \Delta d_5 - \frac{d}{E}\nu\sigma_z^0 \\ \Delta d_6 - \frac{d}{E}\nu\sigma_z^0 \end{pmatrix}}_{\mathbf{b}} = \mathbf{A} \begin{pmatrix} \sigma_x^0 \\ \sigma_y^0 \\ \tau_{xy}^0 \end{pmatrix}, \tag{3.10}$$

where:

$$\mathbf{A} = -\frac{d}{E}\begin{pmatrix} 1+2(1-\nu^2)\cos(2\theta_1) & 1-2(1-\nu^2)\cos(2\theta_1) & 4(1-\nu^2)\sin(2\theta_1) \\ 1+2(1-\nu^2)\cos(2\theta_2) & 1-2(1-\nu^2)\cos(2\theta_2) & 4(1-\nu^2)\sin(2\theta_2) \\ 1+2(1-\nu^2)\cos(2\theta_3) & 1-2(1-\nu^2)\cos(2\theta_3) & 4(1-\nu^2)\sin(2\theta_3) \\ 1+2(1-\nu^2)\cos(2\theta_4) & 1-2(1-\nu^2)\cos(2\theta_4) & 4(1-\nu^2)\sin(2\theta_4) \\ 1+2(1-\nu^2)\cos(2\theta_5) & 1-2(1-\nu^2)\cos(2\theta_5) & 4(1-\nu^2)\sin(2\theta_5) \\ 1+2(1-\nu^2)\cos(2\theta_6) & 1-2(1-\nu^2)\cos(2\theta_6) & 4(1-\nu^2)\sin(2\theta_6) \end{pmatrix}. \tag{3.11}$$

Now the rank of matrix $\mathbf{A}$ is maximal. However, the system is overdetermined since there are six equations and only three variables. Naturally, measuring the change in diameter in three different orientations would be sufficient to determine σ_x^0, σ_y^0, and τ_{xy}^0 (see [8]). The reason for measuring more than three Δd values is to minimize the overall error. The optimal least-squares solution can be expressed [12] as

$$\begin{pmatrix} \sigma_x^0 \\ \sigma_y^0 \\ \tau_{xy}^0 \end{pmatrix} = (\mathbf{A}^{\mathrm{T}}\mathbf{A})^{-1}\mathbf{A}^{\mathrm{T}}\mathbf{b}. \tag{3.12}$$

Every element of matrix $\mathbf{A}$ and vector $\mathbf{b}$ is known, therefore the in situ stress components perpendicular to the axis of the borehole – here: the horizontal components – can be determined. It must be emphasized that these results are just estimations of the real in situ stress state, as several assumptions have been made (see Subsection 3.1.1).

Based on the above, the in situ stress components (σ_x^0, σ_y^0 and τ_{xy}^0) in the plane $(x - y)$ perpendicular to the axis of the borehole can be estimated from the data collected from a single measurement. In order to calculate these estimations, besides the assumptions listed in Subsection 3.1.1, the following values have to be known:

- the change in diameter of the pilot hole (Δd) in at least three different orientations θ,
- the material properties of the rock (ρ, E and ν, as defined previously).

Since the IST gauge measures only radial deformations, the in situ stress state can only be estimated in a plane perpendicular to the axis of the borehole. Furthermore, the axial in situ stress component must be known. In our model, the axis of the borehole is vertical, so it has been assumed that this axial component is the lithostatic pressure (see (3.9)).

It is worth noting that the determination of the axial in situ stress components based purely on measurements is possible using the IST method. However, it requires measurements made in boreholes with different orientations. This method is detailed in [10].

3.2. **Evaluation of CSIRO HI cell measurements.** Unlike the IST instrument, which measures displacements directly, the CSIRO HI cell contains strain gauges, measuring the strains on the surface of the pilot hole during the relief of the rock core. The collected data can subsequently be used to determine the original in situ stress state.

3.2.1. *Assumptions.* In order to derive the in situ stress state from the strains measured on the pilot hole surface, the following assumptions have been made according to [11]:

- the stress state is identical in any plane perpendicular to the axis of the borehole,
- the drilling of the borehole and the pilot hole have no influence on the original in situ stress state,
- after overcoring, the rock core and the surface of the pilot hole are completely relieved from any stress,
- the rock and the CSIRO HI cell is considered to be linearly elastic, homogeneous and isotropic,
- the viscoelastic behaviour of the epoxy resin bonding the cell to the rock is negligible,
- the Young's modulus of the rock and the diameter of the overcoring bit are sufficiently large to neglect the resistance of the HI cell to the deformation.

These are similar to the assumptions listed in Subsection 3.1.1. They imply that the strains measured by the gauges are caused by the relief of the in situ stress state, therefore a connection can be found between them. The stress state can be described in the way given in Subsection 3.1.2.

However, whilst an IST gauge does not provide enough data to determine the in situ stress components parallel to the axis of the borehole, a measurement carried out by a CSIRO HI cell can be used to estimate every component of the in situ stress tensor.

The CSIRO HI cells has variants, that contain either 9 or 12 strain gauges installed in different positions and orientations [11]. In the following, we consider a 12-gauge cell.

3.2.2. *Strain gauge positions.* The positions of the 12 strain gauges are shown in Figure 2 and in Table 1.

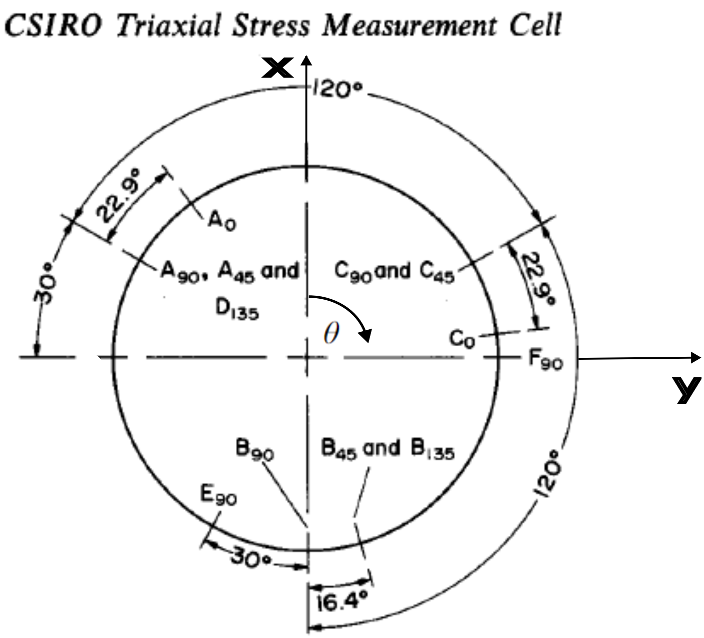

Figure 2. Strain gauge positions in the HI cell [11]

Table 1. Strain gauge positions in the HI cell [13]

ID	θ [°]	β [°]
A_0	323	0
A_{90}	300	90
A_{45}	300	45
B_{45}	163.5	45
B_{135}	163.5	135
B_{90}	180	90
C_0	83	0
C_{90}	60	90
C_{45}	60	45
D_{135}	300	135
E_{90}	210	90
F_{90}	90	90

The angle θ specifies the position of the strain gauge along the perimeter of the pilot hole measured from the x axis. The angle β specifies the orientation of the strain gauge:

- 0°: axial strain (ε_z),
- 90°: tangential strain (ε_θ),
- 45° or 135°: diagonal strain ($\varepsilon_{\pm 45^\circ}$).

Note that whilst the IST gauge measures only radial deformations, the strain gauges in the CSIRO HI cell measure tangential, axial and diagonal strains: this enables each component of the in situ stress tensor to be determined from the measurements performed via the HI cell.

3.2.3. *Connection between stress state and strains.* The in situ stress state associated with the measured strains is given by the following relationships (derived in[11]) as

$$\begin{aligned} E_r\varepsilon_\theta =& -(\sigma_x^0+\sigma_y^0)K_1+ \\ &+2(1-\nu_r^2)\left[(\sigma_x^0-\sigma_y^0)\cos(2\theta)+2\tau_{xy}^0\sin(2\theta)\right]K_2+\nu_r K_4\sigma_z^0, \end{aligned} \tag{3.13}$$

$$E_r\varepsilon_z = -\sigma_z^0+\nu_r(\sigma_x^0+\sigma_y^0), \tag{3.14}$$

$$E_r\gamma_{\theta z} = -4(1+\nu_r)(\tau_{yz}^0\cos 2\theta-\tau_{xz}^0\sin 2\theta)K_3, \tag{3.15}$$

$$\varepsilon_{\pm 45^\circ} = \frac{1}{2}(\varepsilon_z+\varepsilon_\theta\pm\gamma_{\theta z}). \tag{3.16}$$

Variables and parameters contained in these equations:

- E_r and ν_r are the Young's modulus and Poisson's ratio of the rock
- ε_θ, ε_z, and $\varepsilon_{\pm 45^\circ}$ are the tangential, axial and diagonal strains measured by the strain gauges,
- θ is the angle describing the strain gauge position,
- σ_x^0, σ_y^0, σ_z^0, τ_{xy}^0, τ_{xz}^0, τ_{yz}^0 are the elements of the in situ stress tensor (see (3.4))
- $\gamma_{\theta z}$ is the engineering shear strain, which can be calculated according to (3.16),
- K_1, K_2, K_3, K_4 are correction factors, detailed below.

The correction factors are necessary as the strain gauges are located in the stress sensor pipe instead of the pilot hole surface, and the material properties of the CSIRO HI cell are not identical to the material properties of the rock [11]. It is worth emphasizing that the behaviour of the HI cell is considered to be linearly elastic. In certain cases (e.g. high temperature), this assumption is not acceptable since the viscoelastic behaviour of the HI cell must be taken into consideration.

In order to calculate the correction factors, the following values must be known:

- E_p, the Young's modulus of the cell,
- ν_p, the Poisson's ratio of the cell,
- R_p, the radius of the pilot hole,
- R_{sg}, the distance between the strain gauges and the borehole axis,
- R_1, the inner radius of the stress sensor pipe.

For the detailed calculation of the correction factors, see [11].

3.2.4. *Determination of the stress components perpendicular to the borehole axis.* Expressing σ_z from (3.14), then substituting it into (3.13) results in the expression

$$\begin{aligned} E_r(\varepsilon_\theta + \nu_r\varepsilon_z K_4) = &-(\sigma_x^0+\sigma_y^0)K_1 + 2(1-\nu_r^2)\left[(\sigma_x^0-\sigma_y^0)\cos(2\theta) + 2\tau_{xy}^0\sin(2\theta)\right]K_2+ \\ &+\nu_r^2(\sigma_x^0+\sigma_y^0)K_4. \end{aligned} \tag{3.17}$$

Then, equation (3.17) can be used to derive equations for the measurement results given by the strain gauges as

$$\begin{aligned} E_r(\varepsilon_{\theta;\mathrm{A}_{90}} + \nu_r\varepsilon_{z;\mathrm{A}_0}K_4) = &-(\sigma_x^0+\sigma_y^0)K_1+ \\ &+2(1-\nu_r^2)\left[(\sigma_x^0-\sigma_y^0)\cos(2\theta_{\mathrm{A}_{90}}) + 2\tau_{xy}^0\sin(2\theta_{\mathrm{A}_{90}})\right]K_2+ \\ &+\nu_r^2(\sigma_x^0+\sigma_y^0)K_4, \end{aligned} \tag{3.18a}$$

$$\begin{aligned} E_r(\varepsilon_{\theta;\mathrm{B}_{90}} + \nu_r\varepsilon_{z;\mathrm{B}}K_4) = &-(\sigma_x^0+\sigma_y^0)K_1+ \\ &+2(1-\nu_r^2)\left[(\sigma_x^0-\sigma_y^0)\cos(2\theta_{\mathrm{B}_{90}}) + 2\tau_{xy}^0\sin(2\theta_{\mathrm{B}_{90}})\right]K_2+ \\ &+\nu_r^2(\sigma_x^0+\sigma_y^0)K_4, \end{aligned} \tag{3.18b}$$

$$\begin{aligned} E_r(\varepsilon_{\theta;\mathrm{C}_{90}} + \nu_r\varepsilon_{z;\mathrm{C}_0}K_4) = &-(\sigma_x^0+\sigma_y^0)K_1+ \\ &+2(1-\nu_r^2)\left[(\sigma_x^0-\sigma_y^0)\cos(2\theta_{\mathrm{C}_{90}}) + 2\tau_{xy}^0\sin(2\theta_{\mathrm{C}_{90}})\right]K_2+ \\ &+\nu_r^2(\sigma_x^0+\sigma_y^0)K_4, \end{aligned} \tag{3.18c}$$

$$\begin{aligned} E_r(\varepsilon_{\theta;\mathrm{E}_{90}} + \nu_r\varepsilon_{z;\mathrm{B}}K_4) = &-(\sigma_x^0+\sigma_y^0)K_1+ \\ &+2(1-\nu_r^2)\left[(\sigma_x^0-\sigma_y^0)\cos(2\theta_{\mathrm{E}_{90}}) + 2\tau_{xy}^0\sin(2\theta_{\mathrm{E}_{90}})\right]K_2+ \\ &+\nu_r^2(\sigma_x^0+\sigma_y^0)K_4, \end{aligned} \tag{3.18d}$$

$$\begin{aligned} E_r(\varepsilon_{\theta;\mathrm{F}_{90}} + \nu_r\varepsilon_{z;\mathrm{C}_0}K_4) = &-(\sigma_x^0+\sigma_y^0)K_1+ \\ &+2(1-\nu_r^2)\left[(\sigma_x^0-\sigma_y^0)\cos(2\theta_{\mathrm{F}_{90}}) + 2\tau_{xy}^0\sin(2\theta_{\mathrm{F}_{90}})\right]K_2+ \\ &+\nu_r^2(\sigma_x^0+\sigma_y^0)K_4. \end{aligned} \tag{3.18e}$$

The above is a system of linear equations, where σ_x^0, σ_y^0 and τ_{xy}^0 are to be determined. It can be written in a matrix equation form as

$$\underbrace{E_r\begin{pmatrix} \varepsilon_{\theta;\mathrm{A}_{90}} + \nu_r\varepsilon_{z;\mathrm{A}_0}K_4 \\ \varepsilon_{\theta;\mathrm{B}_{90}} + \nu_r\varepsilon_{z;\mathrm{B}}K_4 \\ \varepsilon_{\theta;\mathrm{C}_{90}} + \nu_r\varepsilon_{z;\mathrm{C}_0}K_4 \\ \varepsilon_{\theta;\mathrm{E}_{90}} + \nu_r\varepsilon_{z;\mathrm{B}}K_4 \\ \varepsilon_{\theta;\mathrm{F}_{90}} + \nu_r\varepsilon_{z;\mathrm{C}_0}K_4 \end{pmatrix}}_{\mathbf{d}} = \underbrace{\begin{pmatrix} C_{11} & C_{12} & C_{13} \\ C_{21} & C_{22} & C_{23} \\ C_{31} & C_{32} & C_{33} \\ C_{41} & C_{42} & C_{43} \\ C_{51} & C_{52} & C_{53} \end{pmatrix}}_{\mathbf{C}} \begin{pmatrix} \sigma_x^0 \\ \sigma_y^0 \\ \tau_{xy}^0 \end{pmatrix}, \tag{3.19}$$

where $\varepsilon_{z;\mathrm{B}}$ can be determined using (3.16):

$$\varepsilon_{z;\mathrm{B}} = \frac{\varepsilon_{\mathrm{B}_{45}} + \varepsilon_{\mathrm{B}_{135}}}{2} - \varepsilon_{\mathrm{B}_{90}}. \tag{3.20}$$

The elements of matrix $\mathbf{C}$ are:

$$C_{11} = -K_1 + 2(1-\nu_r^2)\cos(2\theta_{\mathrm{A}_{90}})K_2 + \nu_r^2 K_4, \tag{3.21a}$$

$$C_{12} = -K_1 - 2(1-\nu_r^2)\cos(2\theta_{\mathrm{A}_{90}})K_2 + \nu_r^2 K_4, \tag{3.21b}$$

$$C_{13} = 4(1-\nu_r^2)\sin(2\theta_{\mathrm{A}_{90}}), \tag{3.21c}$$
$$C_{21} = -K_1 + 2(1-\nu_r^2)\cos(2\theta_{\mathrm{B}_{90}})K_2 + \nu_r^2 K_4, \tag{3.21d}$$
$$C_{22} = -K_1 - 2(1-\nu_r^2)\cos(2\theta_{\mathrm{B}_{90}})K_2 + \nu_r^2 K_4, \tag{3.21e}$$
$$C_{23} = 4(1-\nu_r^2)\sin(2\theta_{\mathrm{B}_{90}}), \tag{3.21f}$$
$$C_{31} = -K_1 + 2(1-\nu_r^2)\cos(2\theta_{\mathrm{C}_{90}})K_2 + \nu_r^2 K_4, \tag{3.21g}$$
$$C_{32} = -K_1 - 2(1-\nu_r^2)\cos(2\theta_{\mathrm{C}_{90}})K_2 + \nu_r^2 K_4, \tag{3.21h}$$
$$C_{33} = 4(1-\nu_r^2)\sin(2\theta_{\mathrm{C}_{90}}), \tag{3.21i}$$
$$C_{41} = -K_1 + 2(1-\nu_r^2)\cos(2\theta_{\mathrm{E}_{90}})K_2 + \nu_r^2 K_4, \tag{3.21j}$$
$$C_{42} = -K_1 - 2(1-\nu_r^2)\cos(2\theta_{\mathrm{E}_{90}})K_2 + \nu_r^2 K_4, \tag{3.21k}$$
$$C_{43} = 4(1-\nu_r^2)\sin(2\theta_{\mathrm{E}_{90}}), \tag{3.21l}$$
$$C_{51} = -K_1 + 2(1-\nu_r^2)\cos(2\theta_{\mathrm{F}_{90}})K_2 + \nu_r^2 K_4, \tag{3.21m}$$
$$C_{52} = -K_1 - 2(1-\nu_r^2)\cos(2\theta_{\mathrm{F}_{90}})K_2 + \nu_r^2 K_4, \tag{3.21n}$$
$$C_{53} = 4(1-\nu_r^2)\sin(2\theta_{\mathrm{F}_{90}}). \tag{3.21o}$$

The position of the strain gauges imply that the E_{90} and F_{90} tangential strains belong to the $\varepsilon_{z;\mathrm{B}}$ and $\varepsilon_{z;\mathrm{C}_0}$ axial strains.

The elements of matrix $\mathbf{C}$ and vector $\mathbf{d}$ are known. The system is overdetermined, thus the solution is carried out using the least-squares error method (similarly to the case of the IST method detailed in Subsection 3.1) as

$$\begin{pmatrix} \sigma_x^0 \\ \sigma_y^0 \\ \tau_{xy}^0 \end{pmatrix} = (\mathbf{C}^{\mathrm{T}}\mathbf{C})^{-1}\mathbf{C}^{\mathrm{T}}\mathbf{d}. \tag{3.22}$$

This gives an estimate of the in situ stress state perpendicular to the borehole axis.

3.2.5. *Stress components parallel to the borehole axis.* The axial normal stress component can be calculated according to (3.14) as

$$\sigma_z^0 = \nu_r(\sigma_x^0 + \sigma_y^0) - E_r\varepsilon_z. \tag{3.23}$$

If σ_x^0 and σ_y^0 are known, the above expression can be evaluated. Since there are several measurement values for ε_z, their arithmetic mean is used for the calculations.

The axial shear stresses can be determined using equations (3.15)–(3.16). A linear system of equations can be written for τ_{xz} and τ_{yz} as

$$E_r\gamma_{\theta z;\mathrm{A}_{45}} = -4(1+\nu_r)(\tau_{yz}^0\cos 2\theta_{\mathrm{A}_{45}} - \tau_{xz}^0\sin 2\theta_{\mathrm{A}_{45}})K_3, \tag{3.24a}$$
$$E_r\gamma_{\theta z;\mathrm{B}_{45}} = -4(1+\nu_r)(\tau_{yz}^0\cos 2\theta_{\mathrm{B}_{45}} - \tau_{xz}^0\sin 2\theta_{\mathrm{B}_{45}})K_3, \tag{3.24b}$$
$$E_r\gamma_{\theta z;\mathrm{B}_{135}} = -4(1+\nu_r)(\tau_{yz}^0\cos 2\theta_{\mathrm{B}_{135}} - \tau_{xz}^0\sin 2\theta_{\mathrm{B}_{135}})K_3, \tag{3.24c}$$
$$E_r\gamma_{\theta z;\mathrm{D}_{135}} = -4(1+\nu_r)(\tau_{yz}^0\cos 2\theta_{\mathrm{D}_{135}} - \tau_{xz}^0\sin 2\theta_{\mathrm{D}_{135}})K_3. \tag{3.24d}$$

Expressed in a matrix form as

$$E_r \underbrace{\begin{pmatrix} \gamma_{\theta z;\mathrm{A}_{45}} \\ \gamma_{\theta z;\mathrm{B}_{45}} \\ \gamma_{\theta z;\mathrm{B}_{135}} \\ \gamma_{\theta z;\mathrm{D}_{135}} \end{pmatrix}}_{\mathbf{f}} = \underbrace{-4K_3(1+\nu_r) \begin{pmatrix} -\sin 2\theta_{\mathrm{A}_{45}} & \cos 2\theta_{\mathrm{A}_{45}} \\ -\sin 2\theta_{\mathrm{B}_{45}} & \cos 2\theta_{\mathrm{B}_{45}} \\ -\sin 2\theta_{\mathrm{B}_{135}} & \cos 2\theta_{\mathrm{B}_{135}} \\ -\sin 2\theta_{\mathrm{D}_{135}} & \cos 2\theta_{\mathrm{D}_{135}} \end{pmatrix}}_{\mathbf{E}} \begin{pmatrix} \tau^0_{xz} \\ \tau^0_{yz} \end{pmatrix}. \tag{3.25}$$

Engineering shear strains are calculated according to (3.16). The elements of matrix **E** and vector **f** are known. This equation system is also overdetermined, so the solution is carried out using the least-squares error method again as

$$\begin{bmatrix} \tau^0_{xz} \\ \tau^0_{yz} \end{bmatrix} = (\mathbf{E}^{\mathrm{T}}\mathbf{E})^{-1}\mathbf{E}^{\mathrm{T}}\mathbf{f}, \tag{3.26}$$

giving the remaining components of the in situ stress tensor.

As shown above, a measurement carried out by a CSIRO HI cell provides enough data from a single borehole to estimate every in situ stress component. To summarize, besides the assumptions mentioned in Subsection 3.2.1, this estimation requires the following data:

- tangential strain (ε_θ) values from at least 3 differentθ positions ,
- axial strain (ε_z) value from at least one θ position (measuring at at more than one position provides more reliable results),
- engineering shear strain $\gamma_{\theta z}$ values from at least 2 different θ positions (these can be calculated according to (3.16)),
- material properties of the rock (ρ, E_r and ν_r),
- values required to calculate the correction factors (see Subsection 3.2.3 for details).

4. Finite element models of overcoring measurements

For determining the validity and shortcomings of the assumptions contained in the two measurement methods detailed above, we carry out finite element simulations of two respective models of overcoring measurement. In situ stress components – given as boundary conditions – and material properties are specified according to the results of a measurement carried out at the National Radioactive Waste Repository in Bátaapáti, Hungary [14, 15]. Based on the deformation and strain results of the simulation, an estimation of the in situ stress state is calculated according to the formulas given in Sections 3.1–3.2. Then, we compare these estimations to the values specified initially as boundary conditions, in order to examine the accuracy of these techniques, and to determine the optimal location of the measuring instrument.

4.1. **Finite element model of the IST measurement.** The finite element analysis was carried out using ANSYS Mechanical. In accordance with the linear elastic material model assumed and the evaluation procedure of the IST method, we performed three static analyses, each representing one of the three steps of an overcoring measurement. We modelled a sufficiently large domain of rock at a depth of 276 m, loaded by the in situ stress state. (The depth and the loads were chosen according to [14].) Due to the symmetry of the geometry and the loads, a quarter model was used. It should be noted that the use of an axisymmetric model is not suitable here, as the in-situ stress state is usually not hydrostatic [1]. This is modelled according to Section 4.1.3.

The evaluation of the results from the finite element model (FEM) was carried out as detailed in Section 3.1. The aim of the investigation was to ascertain whether it is possible to determine the in situ stress state from the data collected during an IST measurement and, if so, how accurately the in situ stress components can be estimated.

4.1.1. *Geometry.* The simulation domain is represented as a cuboid. The longest edges of this cuboid are parallel to z, representing the vertical direction. The height of the cuboid is 2400 mm, and the vertical edges are all 600 mm long. With these dimensions, the disturbance in the stress field caused by the borehole is negligible on the side faces of the cuboid. The boreholes are modelled as cylinders with vertical axes intersecting the horizontal faces at their centers. The hole diameters are the following:

- borehole: 96 mm,
- pilot hole: 25.5 mm,
- overcoring, inner diameter: 63 mm,
- overcoring, outer diameter: 96 mm.

In order to decrease the computational resources required for the computations a quarter model was made. The model was divided into different bodies at the hole bottoms, making structured mesh generation feasible. After slicing, one part was formed from the bodies, merging the nodes on the contacting faces.

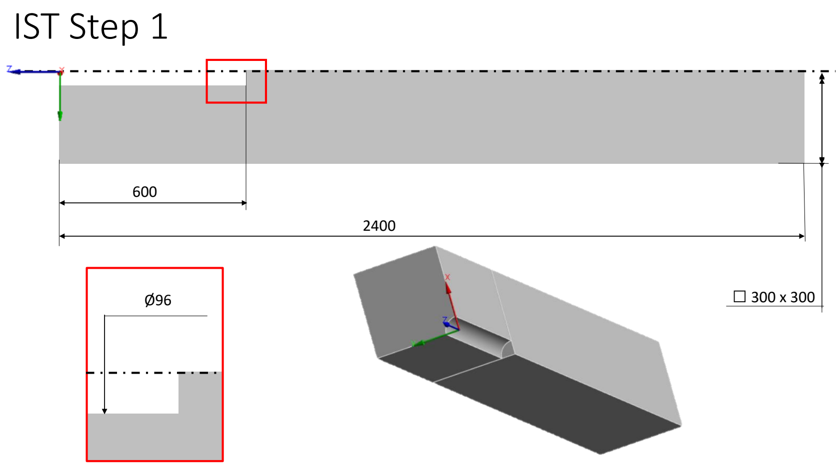

Figure 3. Applied geometry for modelling Step 1 of the IST measurement

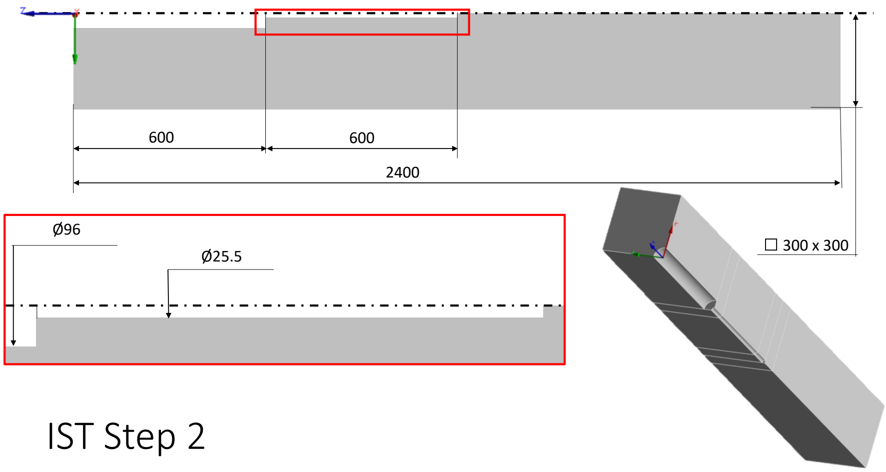

Figure 4. Applied geometry for modelling Step 2 of the IST measurement

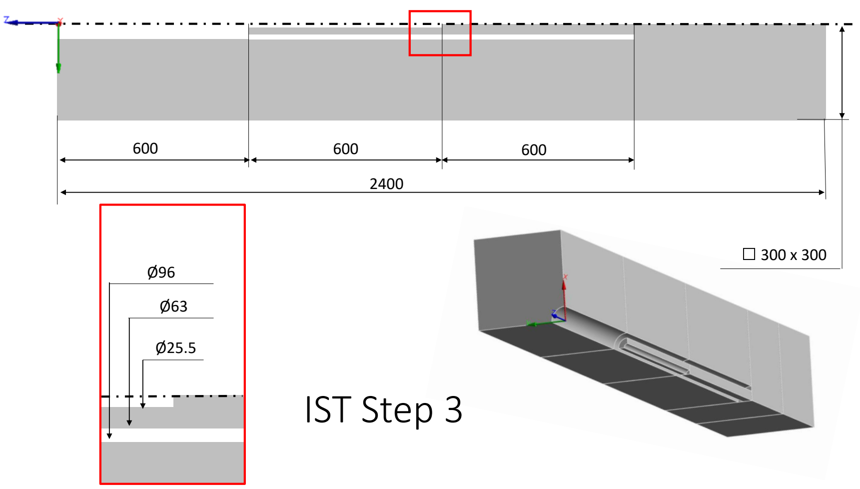

Figure 5. Applied geometry for modelling Step 3 of the IST measurement

The geometry applied for each step is presented in Figures 3–5. The origin of the global coordinate system is at the intersection of the borehole axis and the upper horizontal face.

4.1.2. *Finite element mesh.* The finite element mesh has been generated by ANSYS Mechanical. During the simulation of all three steps, identical principles were followed. Hexagonal elements were used to minimize the number of elements, and smaller elements were generated near the bottoms of the holes, as the deformation and stress change abruptly at these locations. MultiZone meshing method was applied with element sizes being

- near the holes: 2–3 mm,
- far from the holes: 12–15 mm.

The applied meshes are presented in Figs. 6–8.

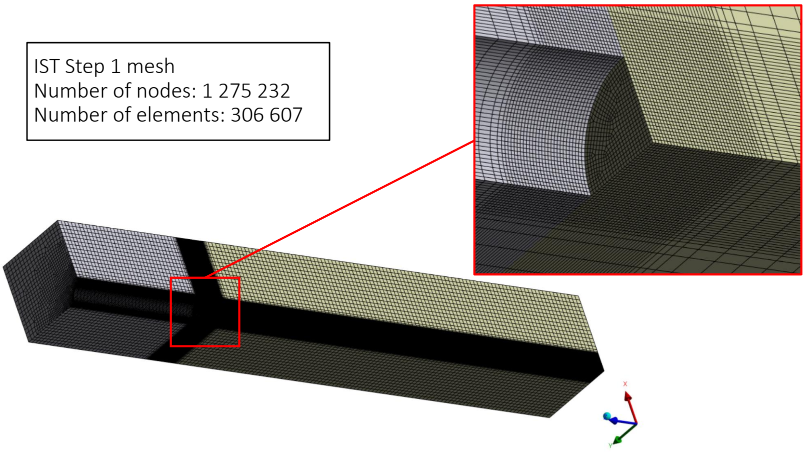

Figure 6. Applied finite element mesh for modelling Step 1 of the IST measurement

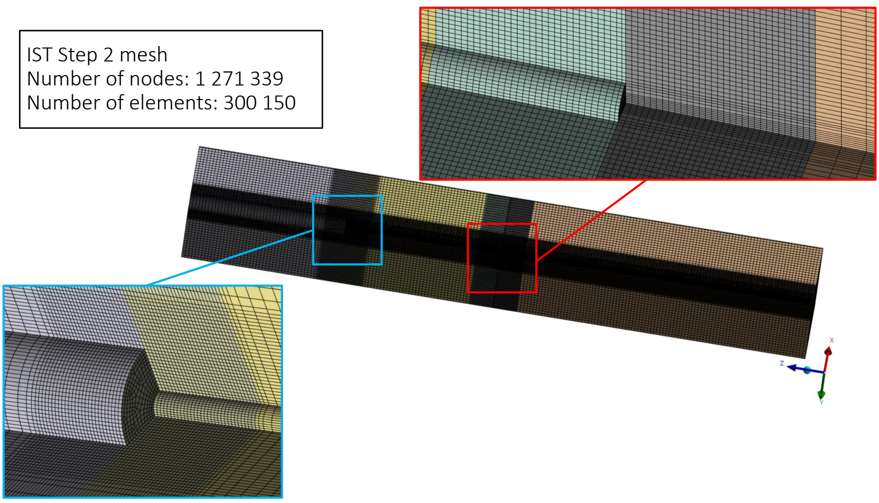

Figure 7. Applied finite element mesh for modelling Step 2 of the IST measurement

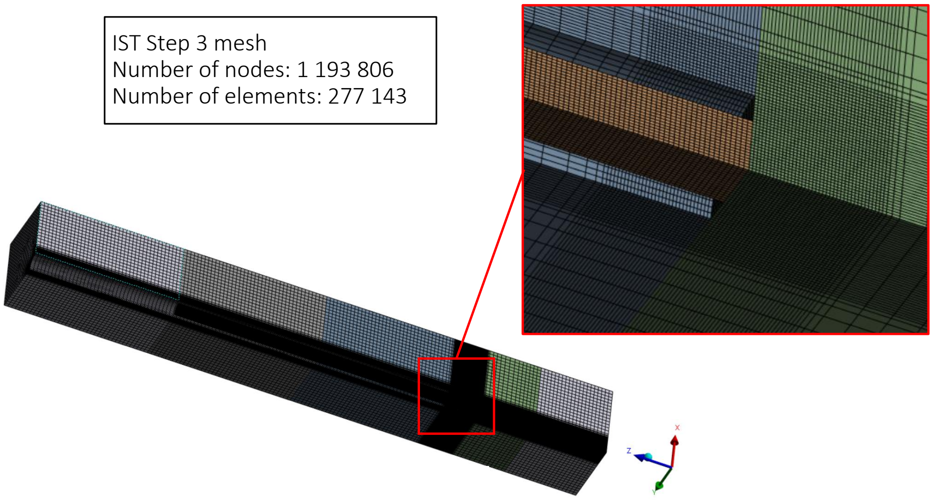

Figure 8. Applied finite element mesh for modelling Step 3 of the IST measurement

4.1.3. *Material properties and boundary conditions.* Material properties and boundary conditions are defined according to the results of the measurements carried out at the National Radioactive Waste Repository in Bátaapáti, Hungary [14, 15]. The rock (porphyric monzogranite) is considered to be linearly elastic with the following properties:

- Young's modulus: 73.62 GPa,
- density: 2732 $\mathrm{kg/m^3}$,
- Poisson's ratio: 0.253.

The modelled domain is located at a depth of 276 m and loaded by the in situ stress state. At this point, the following assumptions are made:

- the modelled domain is large enough, so that the load of the outer surface of it is considered to be identical in every step,
- the vertical normal in situ stress component is the lithostatic pressure (see (3.9)).

Using the assumptions above, the load of the model can be given as three pressure boundary conditions acting on the outer surface of the modelled domain. The values of these during each step:

$$p_x = 8.21\,\mathrm{MPa}, \tag{4.1}$$

$$p_y = 7\,\mathrm{MPa}, \tag{4.2}$$

$$p_z = 7.5\,\mathrm{MPa}. \tag{4.3}$$

Please note that the p_z value is larger than it should be according to (3.9). The reason behind this is the difference between the areas of the horizontal faces: the upper face is smaller due to the presence of the borehole. The pressure p_z is applied on the upper face.

The constraints of the modelled domain are the following:

- symmetry is applied on the $x - z$ and $y - z$ planes: no node in these planes can move perpendicular to the plane,
- for every node in the lower horizontal face the displacement in z direction is set to be zero.

The applied boundary conditions are shown in Figure 9. It is worth noting that while formulating the finite element models, several methods of constraining the rigid body motion in z direction were tested. One of these was setting the z displacement of the faces loaded by pressure in the x and y directions to be zero. However, the results (especially for σ_z) implied that the best solution is constraining the lower horizontal face, as shown here.

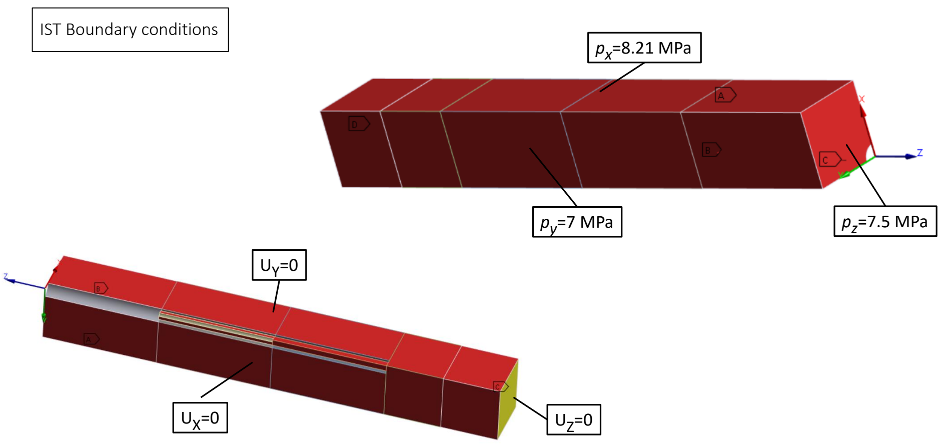

Figure 9. Boundary conditions applied during simulation of the IST measurement

4.1.4. *Evaluation.* As described in Section 3.1, the IST gauge measures the changes in diameter of the pilot hole during overcoring in six different orientations and depths. The aim of the evaluation performed here is to construct the in situ stress tensor from the virtual measurement data provided by the finite element results, as detailed in Section 3.1. Hence, the radial displacement of the points of the pilot hole surface has been queried in Steps 2 and 3. This simulates a measurement with ideal circumstances.

IST Path details

Path name	Orientation [°]	Start point coordinates			End point coordinates		
		x [mm]	y [mm]	z [mm]	x [mm]	y [mm]	z [mm]
path_0°	0	12.750	0	-600	12.750	0	-1200
path_30°	30	11.042	6.375	-600	11.042	6.375	-1200
path_60°	60	6.375	11.042	-600	6.375	11.042	-1200
path_90°	90	0	12.750	-600	0	12.750	-1200

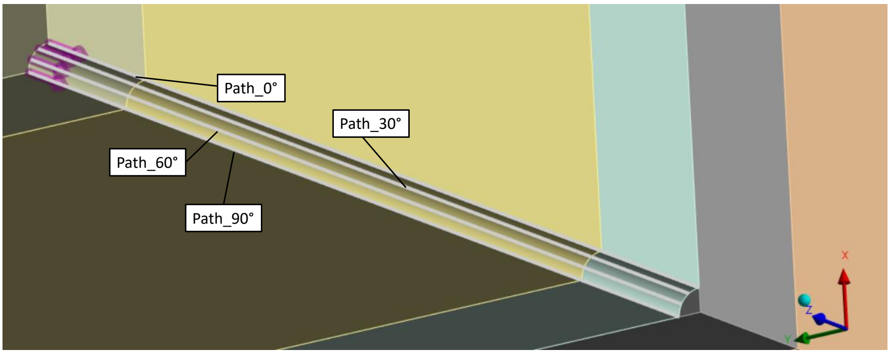

Figure 10. Paths defined to evaluate the simulation of the IST measurement. The paths are given with the global coordinates of the start and end points.

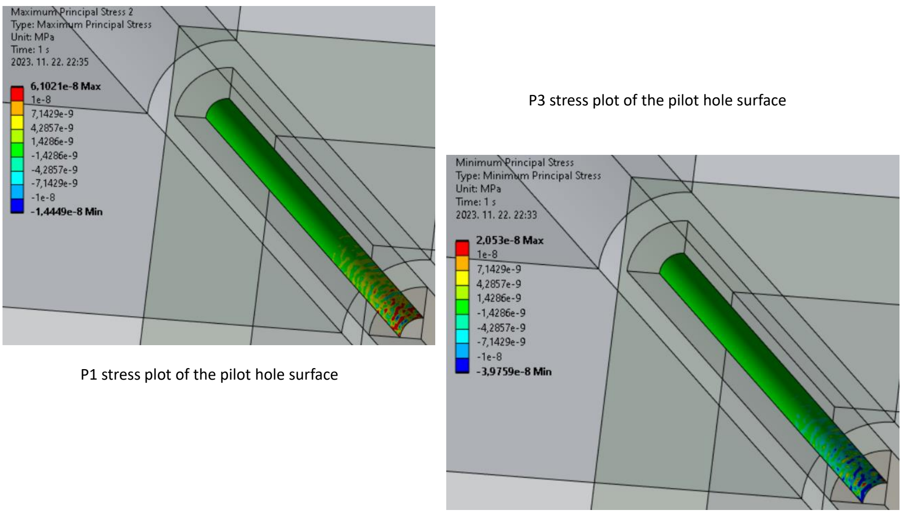

Figure 11. P1 and P3 stress results from Step 3 of the IST simulation. The minimal and maximal values imply that the pilot hole is relieved in this step.

Paths have been defined on the pilot hole surface along the full length of the hole in several orientations θ, as depicted in Figure 10. A real IST gauge measures the change of six diameters, forming a 30-degree angle. Since a quarter model is used, only four of these are investigated, because the other two do not give any further results. Consequently, the paths are defined at orientations $\theta = 0°$, $\theta = 30°$, $\theta = 60°$ and $\theta = 90°$, where θ is the angle formed by the measured diameter and the x axis of the global coordinate system. The distance of the pins in the IST gauge is 10–15 mm [16], so the distance between the points where the radial displacements are queried is 12.5 mm.

This provides the radial displacement of the points on the pilot hole surface caused by the in situ stress state in each step. In Step 2, this stress state loads the pilot hole surface. However, in Step 3, the remaining rock core, which contains the pilot hole, is relieved from any stress. This is shown in Figure 11.

The diameter change of the pilot hole during the relief in any orientation can be calculated as (taking symmetry into account):

$$\Delta d = 2(U_{rad}^{[3]} - U_{rad}^{[2]}), \tag{4.4}$$

where $U_{rad}^{[2]}$ and $U_{rad}^{[3]}$ are the radial displacements of the pilot hole surface calculated from the FEM in Steps 2 and 3. Since the pilot hole is assumed to be relieved from any stress in Step 3,

$$U_{rad}^{[3]} = 0, \tag{4.5}$$

thus the change in diameter becomes

$$\Delta d = -2U_{rad}^{[2]}. \tag{4.6}$$

Based on (4.6), the changes in diameter along the paths presented in Figure 10 can be evaluated. These changes in diameter are shown in Figure 12.

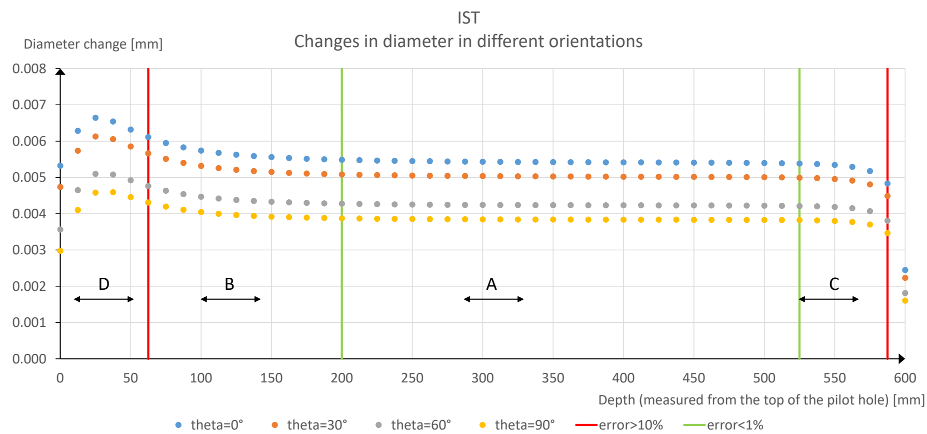

Figure 12. Diameter change Δd results of the IST simulation in each orientation. Red and green lines represent the error correlating to the Δd result from the middle of the pilot hole. The intervals labelled with letters are the locations of the simulated measurements.

The in situ stress state can be derived from the diameter changes according to equations (3.10)–(3.12). Due to the symmetry, the last two rows of matrix **A** and vector **b** are not considered. To solve these equations, the following values are needed:

- E and ν material properties (see Subsection 4.1.3),
- pilot hole diameter: $d = 25.5\,\mathrm{mm}$,
- vertical normal in situ stress component according to equation (3.9): $\sigma_z^0 = -7.5\,\mathrm{MPa}$,
- angles describing the different orientations: $\theta_1 = 0°$, $\theta_2 = 30°$, $\theta_3 = 60°$, $\theta_4 = 90°$,
- Δd diameter changes in each orientation.

The diameter changes depend on the depth measured from the top of the pilot hole, as presented in Figure 12. Firstly, let us substitute Δd values from location A (287–325 mm) into the equations. Doing so, a measurement carried out at such depth is simulated. This location is between the two green lines representing optimal instrument placement in Figure 12. The substituted values are presented in Table 2.

Table 2. Δd values substituted into equation (3.10), from location A (cf. Figure 12).

θ [°]	Depth [mm]	Δd [mm]
0	287.5	$5.437 \cdot 10^{-3}$
30	300	$5.037 \cdot 10^{-3}$
60	312.5	$4.240 \cdot 10^{-3}$
90	325	$3.842 \cdot 10^{-3}$

In situ stress components derived from the Δd values above, and their comparison against the loads set in the model are shown in Table 3. It can be seen that the error of the in situ stress components given by the solution of (3.10) is less than 1%. As a consequence, the estimation error is minimal if the data is collected from location A.

Table 3. Comparison of the in situ stress components derived from the data presented in Table 2., and the loads applied to the model detailed in Subsection 4.1.3.

Stress component	Estimation [MPa]	Load [MPa]	Error
σ_x^0	−8.261	−8.21	0.62%
σ_y^0	−7.031	−7.00	0.45%
τ_{xy}^0	0.001	0	–

Secondly, let us substitute Δd values from location B (100–137.5 mm) into the equations. This location is between the red and green lines shown in Figure 12, i.e., in the 10 % and 1% error range. The substituted values are presented in Table 4.

Table 4. Δd values substituted into equation (3.10), from location B (c.f. Figure 12)

θ [°]	Depth [mm]	Δd [mm]
0	100	$5.742 \cdot 10^{-3}$
30	112.5	$5.258 \cdot 10^{-3}$
60	125	$4.381 \cdot 10^{-3}$
90	137.5	$3.940 \cdot 10^{-3}$

In situ stress components derived from the Δd values above, and their comparison against the loads set in the model are shown in Table 5. It can be seen that the error of the in situ stress components given by the solution of (3.10) is around 5%.

Table 5. Comparison of the in situ stress components derived from the data presented in Table 4 and the loads applied to the model detailed in Subsection 4.1.3

Stress component	Estimation [MPa]	Load [MPa]	Error
σ_x^0	-8.628	-8.21	5.09%
σ_y^0	-7.246	-7.00	3.51%
τ_{xy}^0	0.019	0	–

Now, we substitute Δd values from location C (537.5–575 mm) into the equations. This location is between the green and red lines to the right in Figure 12. The substituted values are presented in Table 6.

Table 6. Δd values substituted into equation (3.10), from location C (c.f. Figure 12)

θ [°]	Depth [mm]	Δd [mm]
0	537.5	$5.369 \cdot 10^{-3}$
30	550	$4.958 \cdot 10^{-3}$
60	562.5	$4.153 \cdot 10^{-3}$
90	575	$3.701 \cdot 10^{-3}$

In situ stress components derived from the Δd values above, and their comparison against the loads set in the model are shown in Table 7. It can be seen that the error of the in situ stress components given by the solution of (3.10) is less than 5%.

The three cases cases illustrate that a good estimation can be given for the in situ stress components, if the Δd values are from a location between the two red lines shown in Figure 12.

Table 7. Comparison of the in situ stress components derived from the data presented in Table 6 and the loads applied to the model detailed in Subsection 4.1.3.

Stress component	Estimation [MPa]	Load [MPa]	Error
σ_x^0	−8.133	−8.21	0.94%
σ_y^0	−6.857	−7.00	2.04%
τ_{xy}^0	−0.018	0.00	–

However, if the estimation is based on Δd values collected outside this interval, the error is significant. The increased error is caused by the disturbed stress and displacement field near the bottom of the boreholes. As an example, we substitute Δd values from location D (12.5–50 mm) into the equations. This location is outside the interval marked by the two red lines according to Figure 12. The substituted values are presented in Table 8.

Table 8. Δd values substituted into equation (3.10), from location D (c.f. Figure 12).

θ [°]	Depth [mm]	Δd [mm]
0	12.5	$6.284 \cdot 10^{-3}$
30	25	$6.123 \cdot 10^{-3}$
60	37.5	$5.082 \cdot 10^{-3}$
90	50	$4.457 \cdot 10^{-3}$

In situ stress components derived from the Δd values above and their comparison against the loads set in the model are shown in Table 9. It can be seen that the error of the in situ stress components given by the solution of (3.10) exceeds 10%.

Table 9. Comparison of the in situ stress components derived from the data presented in Table 8 and the loads applied to the model written in Subsection 4.1.3

Stress component	Estimation [MPa]	Load [MPa]	Error
σ_x^0	−9.427	−8.21	14.82%
σ_y^0	−7.976	−7.00	13.94%
τ_{xy}^0	−0.209	0.00	–

4.1.5. *Summary of IST simulation results.* Based on the results of the finite element analysis, the in situ stress components can be estimated from the changes in diameter of the pilot hole as written in Section 3.1. Another conclusion is that the location of the IST gauge in the pilot hole has a significant influence on the results. The simulation shows that the ideal position of the IST gauge is between the two green lines in

Figure 12, which means a depth between 200–525 mm, measured from the top of the pilot hole. Nondimensionalizing the depths by the borehole diameter ($D = 96\,\mathrm{mm}$) produces the following results: in order to make the best approximation, the IST gauge should be located at least $2.1D$ beneath the bottom of the borehole, and at least $0.8D$ above the bottom of the pilot hole.

Locating a gauge outside the interval marked by the two red lines in Figure 12 increases the error. In terms of dimensionless values, this means the IST gauge must be located at least $0.7D$ beneath the bottom of the borehole, and $0.1D$ above the bottom of the pilot hole in order to get an acceptable estimation. This agrees with [8, p. 5], which suggests the following: "the plane of the deformation measurement should be located $1D$ ahead of the larger hole". If this $1D$ distance is provided between the gauge and the top of the pilot hole, the error of the estimation is less than 10%. This location is marked with B in Figure 12. The in situ stress components in the horizontal $x - y$ plane can be estimated with an error less than 10% from the data collected at this location (see Table 5).

The same standard [8] suggests that when a distance of $1D$ cannot be left between the IST gauge and the top of the pilot hole, the gauge should be located as far ahead of the larger hole as possible. This also agrees with the simulation results: the distance to be left between the gauge and the bottom of the pilot hole ($0.1D$) is far less than the distance which has be left between the top of the pilot hole and the gauge ($0.7D$).

Furthermore, the assumption made in Subsection 3.1.1 regarding the stress state of the pilot hole at the end of the overcoring is correct based on the results of the simulation (see Figure 11).

4.1.6. *Plausibility check.* In order to prove the results of the FE model plausible, the force equilibrium has been checked. The vector of the loading forces:

$$\mathbf{F_t} = \begin{bmatrix} p_x A_x \\ p_y A_y \\ p_z A_z \end{bmatrix} = \begin{bmatrix} -5\ 911\ 200 \\ -5\ 040\ 000 \\ -661\ 500 \end{bmatrix} \mathrm{N}. \tag{4.7}$$

In these equations, A_x, A_y and A_z are the surfaces on which the pressure boundary conditions were defined. The vector of the reaction forces computed from the FEM:

$$\mathbf{F_r} = \begin{bmatrix} 5\ 911\ 200 \\ 5\ 040\ 000 \\ 661\ 430 \end{bmatrix} \mathrm{N}. \tag{4.8}$$

The sum of the loading and the reaction forces:

$$\mathbf{F_t} + \mathbf{F_r} = \begin{bmatrix} 0 \\ 0 \\ -70 \end{bmatrix} \mathrm{N}. \tag{4.9}$$

This sum has to be zero. Since $-70\,\mathrm{N}$ is negligible, it can be stated that the reaction forces and the defined loads are in equilibrium.

Besides the reaction forces, the stress field on the borehole surface has been checked. At points which can move along the x direction, σ_x has to be zero. Also at points which can move along the y direction, σ_y has to be zero. As shown in Figure 13 the results of the FE model meet these two criteria.

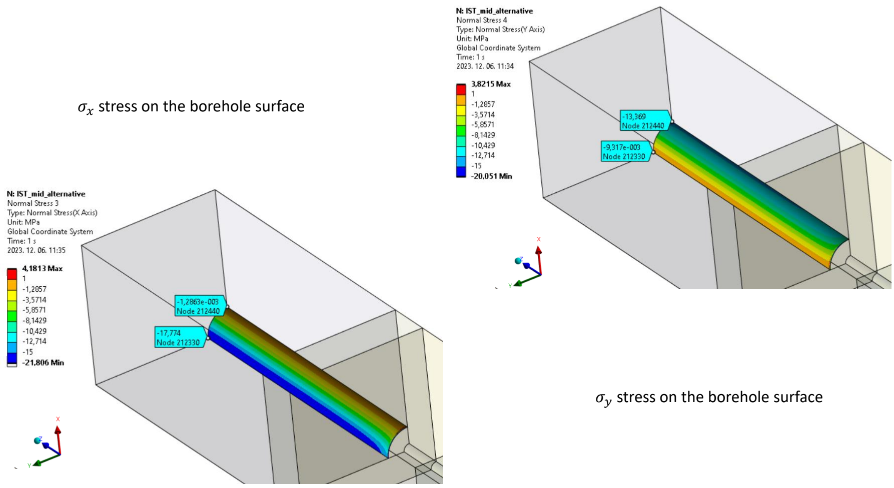

Figure 13. σ_x and σ_y stresses on the borehole surface in Step 2 of the IST simulation

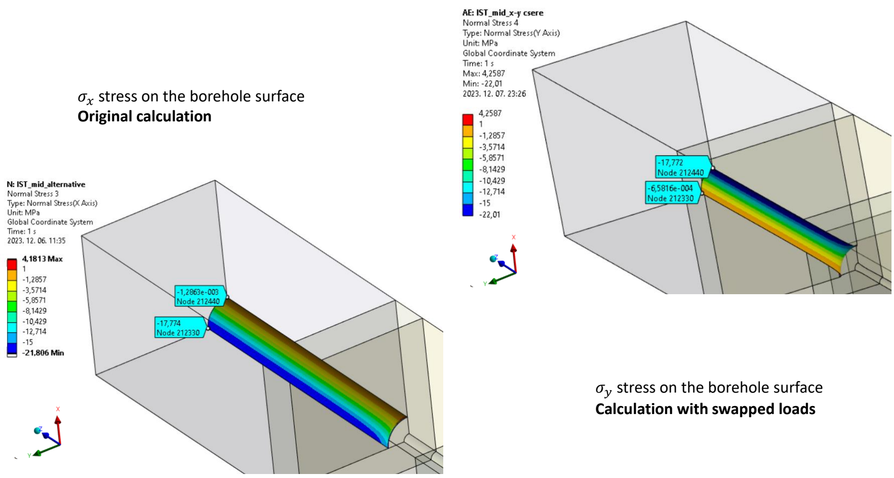

Figure 14. σ_x (left) results of the original simulation and σ_y (right) results of the simulation carried out with the commuted loads

Furthermore, an analysis with p_x and p_y values commuted was carried out and the stress state of the borehole surface was investigated. The commutation of the loads also commutes the x and y axes. This means the σ_x results of the original computation must be the same as the σ_y results of this new simulation. Based on Figure 14, the results of the FE model meet this criterion. Naturally, the results must be mirrored to the plane defined by the z axis and the $x = y$ line.

The plausibility checks were carried out on the results of Step 2 of the IST simulation, since these results are used to derive the in situ stress state. Based on the performed plausibility checks, the results of the FE model are shown to be plausible.

4.2. **Finite element model of the CSIRO HI measurement.** For the CSIRO HI measurement method, the finite element analysis was carried out similarly to the previously described analysis. Three static analyses was performed using ANSYS Mechanical on a large domain of rock at a depth of 276 m and loaded by the in situ stress state, as detailed in Section 4.1. Due to the symmetry of the geometry and the loads, a quarter model can be used here as well. The evaluation of the simulation results was carried out as in Section 3.2. Similarly to the previous analysis, the goal was to determine whether it is possible to determine the in situ stress state from the data collected during a measurement carried out using a CSIRO HI cell, and if so, to determine how accurately the in situ stress components can be estimated.

4.2.1. *Geometry.* The geometric model is similar to that used for simulating the IST measurement. The differences from the model described in Subsection 4.1.1 are the diameters of the holes, which were specified according to [14] as

- borehole : 146 mm,
- pilot hole : 37.7 mm,
- overcoring, inner diameter: 131.4 mm,
- overcoring, outer diameter: 146 mm.

The applied geometry for each step is presented in Figs. 15–17.

4.2.2. *Finite element mesh.* The finite element mesh was generated similarly to the previous analysis, with a slightly different range of element sizes in the MultiZone meshing to accommodate for the different geometry. These element sizes were

- near the holes: 2.5–5 mm,
- far from the holes: 15–17 mm.

The applied meshes are presented in Figures 18–20.

4.2.3. *Material properties and boundary conditions.* The material properties and boundary conditions are the same as those given in Subsection 4.1.3. The applied boundary conditions are shown in Figure 21.

4.2.4. *Evaluation.* As described in Section 3.2, the strain gauges in the CSIRO HI cell measure the strains on the surface of the pilot hole during overcoring in 12 different orientations and positions. The aim is to construct the in situ stress tensor from the virtual measurement data provided by the finite element results as written in Section 3.2. Hence, the strains of the points of the pilot hole surface were queried in Steps 2 and 3. This simulates a measurement in ideal circumstances.

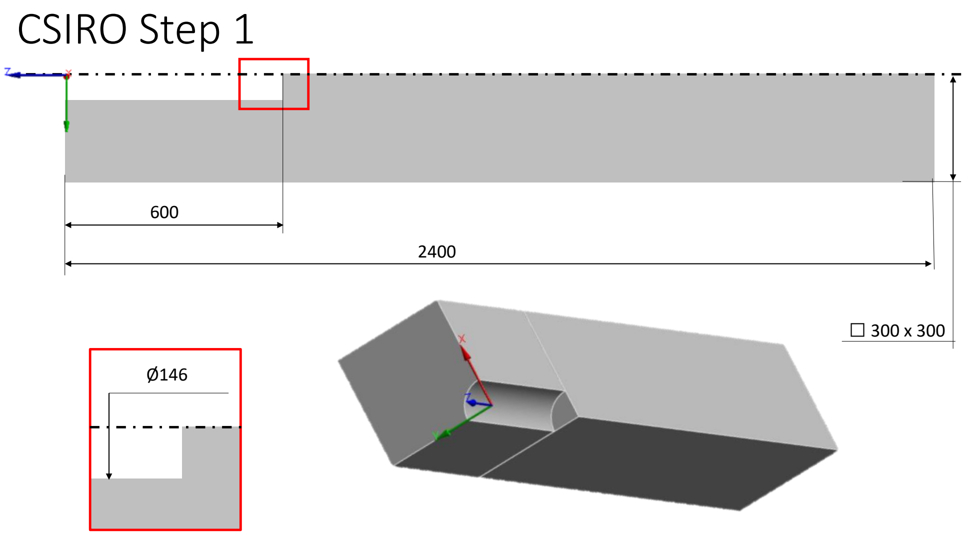

Figure 15. Applied geometry for modelling Step 1 of the CSIRO measurement

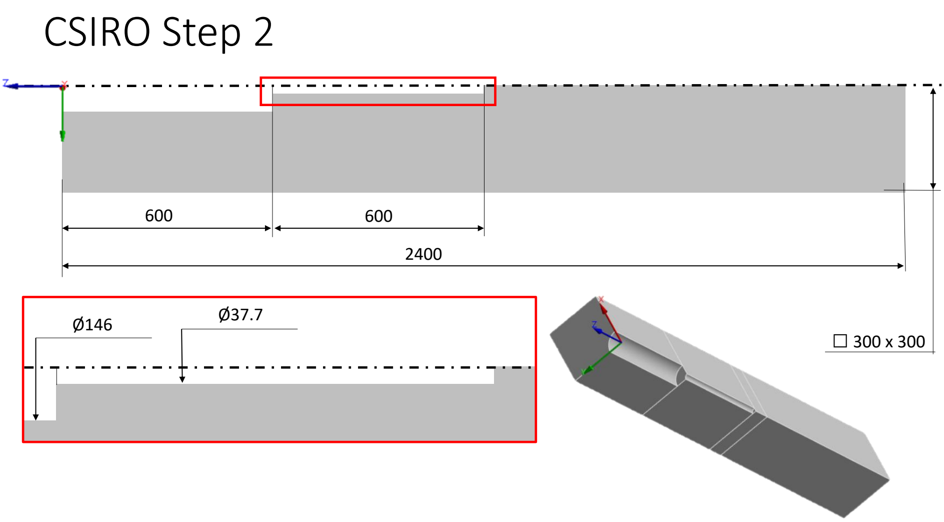

Figure 16. Applied geometry for modelling Step 2 of the CSIRO measurement

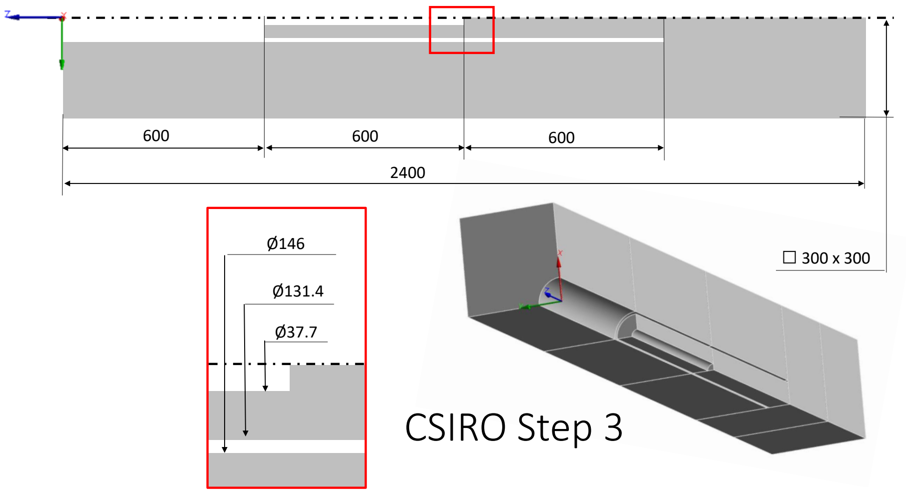

Figure 17. Applied geometry for modelling Step 3 the of CSIRO measurement

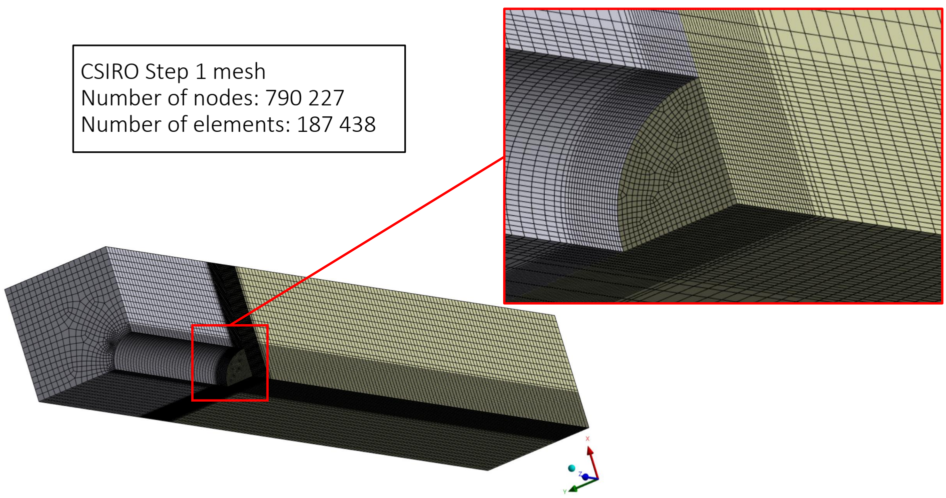

Figure 18. Applied finite element mesh for modelling Step 1 of the CSIRO measurement

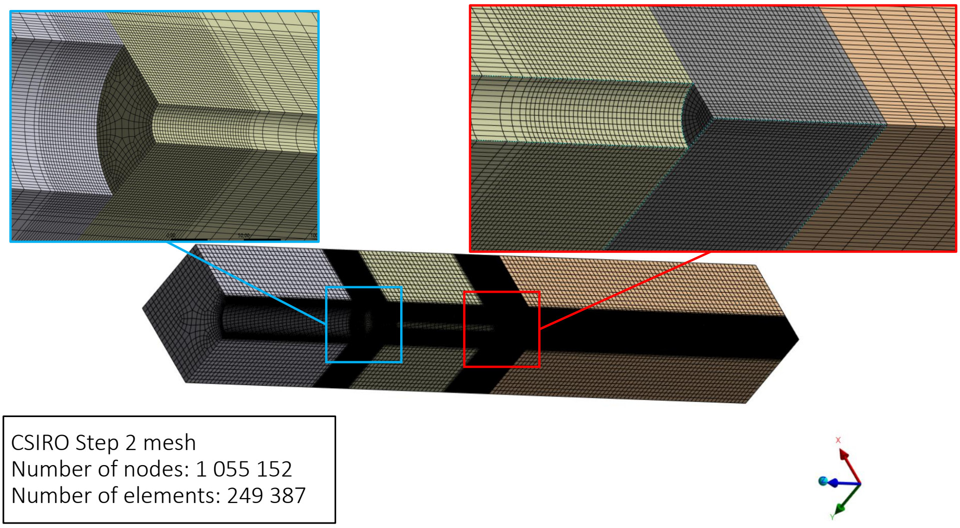

Figure 19. Applied finite element mesh for modelling Step 2 of the CSIRO measurement

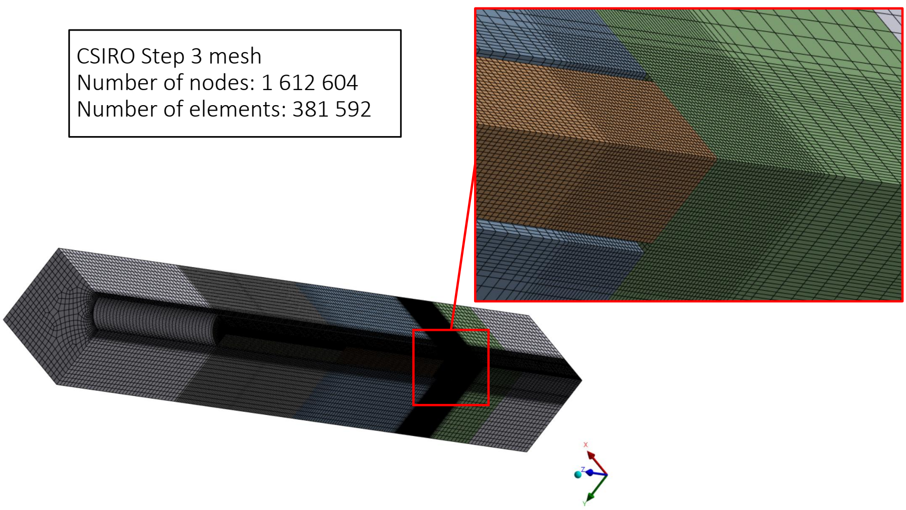

Figure 20. Applied finite element mesh for modelling Step 3 of the CSIRO measurement

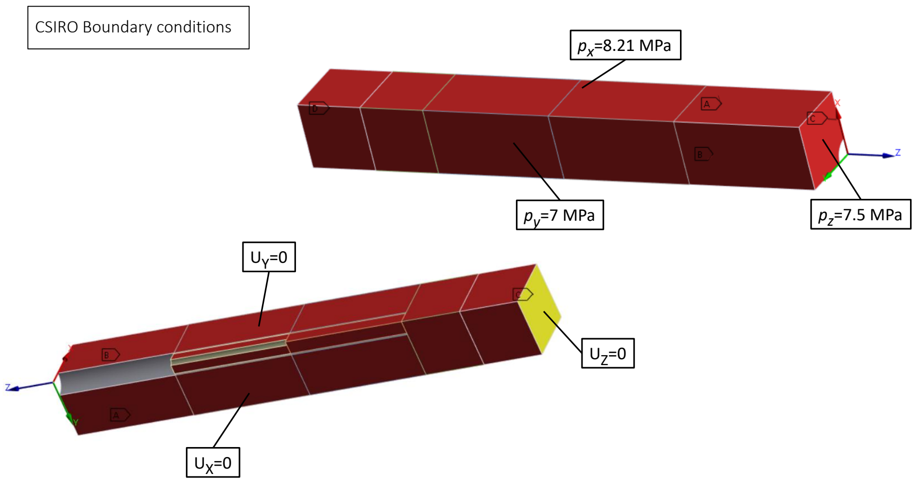

Figure 21. Boundary conditions applied for the simulation of the CSIRO measurement

The positions and orientations of the strain gauges are detailed in Table 1. Since a quarter model was used, the positions change to the values shown in Table 10. The orientation (β) of the strain gauges are not affected by the mirrorings. The following gauges measure the same strain in the quarter model:

- A_{90} and C_{90},
- A_{45} and C_{45}.

The strains measured by these gauges are only considered once during the evaluation.

Table 10. Strain gauge positions in the quarter model [13]

ID	Original θ [°]	Modified θ [°]
A_0	323	37
A_{90}	300	60
A_{45}	300	60
B_{45}	163.5	16.5
B_{135}	163.5	16.5
B_{90}	180	0
C_0	83	83
C_{90}	60	60
C_{45}	60	60
D_{135}	300	60
E_{90}	210	30
F_{90}	90	90

Paths have been defined on the pilot hole surface along the full length of the hole in the modified positions θ as depicted in Figure 22. Along these paths, ε_θ, ε_z and $\gamma_{\theta z}$ are queried in Steps 2 and 3. The difference in these is the strain measured by the gauges during overcoring:

$$\boldsymbol{\Delta\varepsilon} = \boldsymbol{\varepsilon}^{[\mathbf{3}]} - \boldsymbol{\varepsilon}^{[\mathbf{2}]}, \tag{4.10}$$

where $\boldsymbol{\varepsilon}$ tensor describes the strain state of a point of the pilot hole surface.

As mentioned earlier, by the end of the measurement (Step 3), the pilot hole surface is relieved from any stress, which means:

$$\boldsymbol{\varepsilon}^{[\mathbf{3}]} = \mathbf{0}, \tag{4.11}$$

hence strain caused by the relief from the in situ stress state:

$$\boldsymbol{\Delta\varepsilon} = -\boldsymbol{\varepsilon}^{[\mathbf{2}]}. \tag{4.12}$$

The evaluation detailed in Section 3.2 was carried out with these results.

CSIRO Path details

Path name	Position [°]	Start point coordinates			End point coordinates		
		x [mm]	y [mm]	z [mm]	x [mm]	y [mm]	z [mm]
path_0°	0	18.750	0.000	-600	18.750	0.000	-1200
path_16.5°	16.5	17.978	5.325	-600	17.978	5.325	-1200
path_30°	30	16.238	9.375	-600	16.238	9.375	-1200
path_37°	37	14.974	11.284	-600	14.974	11.284	-1200
path_60°	60	9.375	16.238	-600	9.375	16.238	-1200
path_83°	83	2.285	18.610	-600	2.285	18.610	-1200
path_90°	90	0.000	18.750	-600	0.000	18.750	-1200

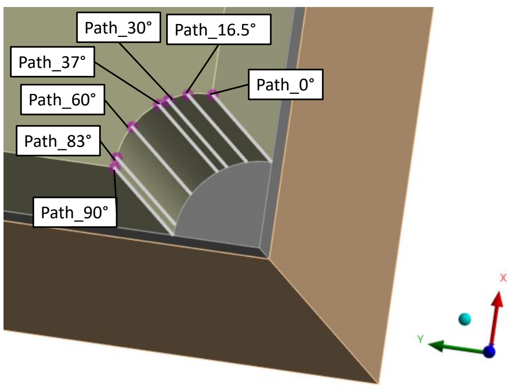

Figure 22. Paths defined to evaluate the simulation of the CSIRO measurement. The paths are given with the global coordinates of the start and end points.

As detailed in Section 4.1., the in situ stress components determined by an IST measurement depend on the location of the gauge in the pilot hole. The same dependence exists in case of the CSIRO HI cell. Tangential strain results are presented in Figure 23.

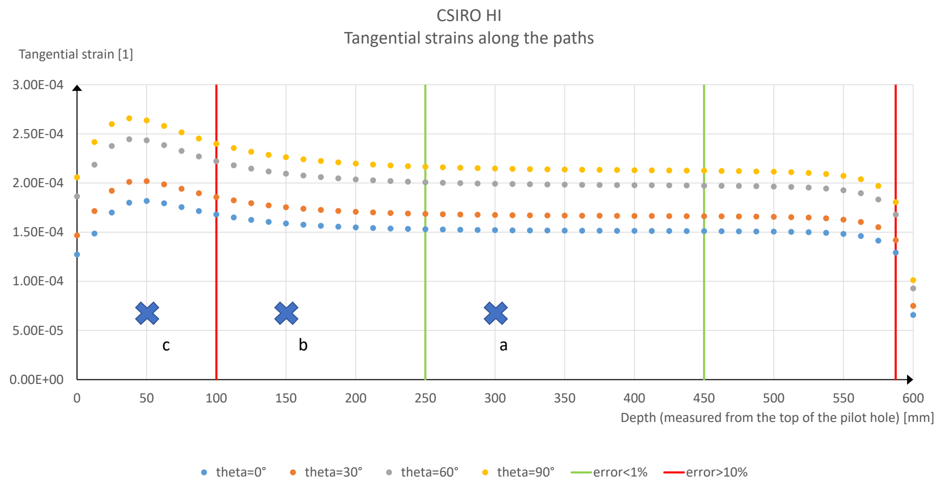

Figure 23. Tangential strain ε_θ results of the CSIRO simulation in each position. Red and green lines represent the error correlating to the ε_θ result from the middle of the pilot hole. The points marked with a cross are the locations of the simulated measurements.

Axial strain results are presented in Figure 24. In the modelled case, the ε_z axial strains are independent from the gauge position θ.

The in situ stress components in the horizontal $(x - y)$ plane can be derived from the strains according to equations (3.19)–(3.22). Due to the symmetry, the 3rd row of matrix **C** and vector **d** are not considered. To solve these equations, the following values are needed:

- E_r and ν_r material properties (Subsection 4.2.3),
- positions and orientations of the strain gauges (Table 10),
- strain results of the simulation, queried at the locations of the strain gauges,
- K_1, K_2, K_4 correction factors. K_3 is only needed to calculate the shear stresses.

In Subsection 3.2.3 the role and calculation of the correction factors are detailed. Since the CSIRO HI cell itself is not modelled, its material properties are considered to be

- $E_p = 0$,
- $\nu_p = 0$.

In the finite element model, the measured strains are queried from the pilot hole surface, hence:

$$R_p = R_{sg} = R_1 = 18.85 \text{ mm} \tag{4.13}$$

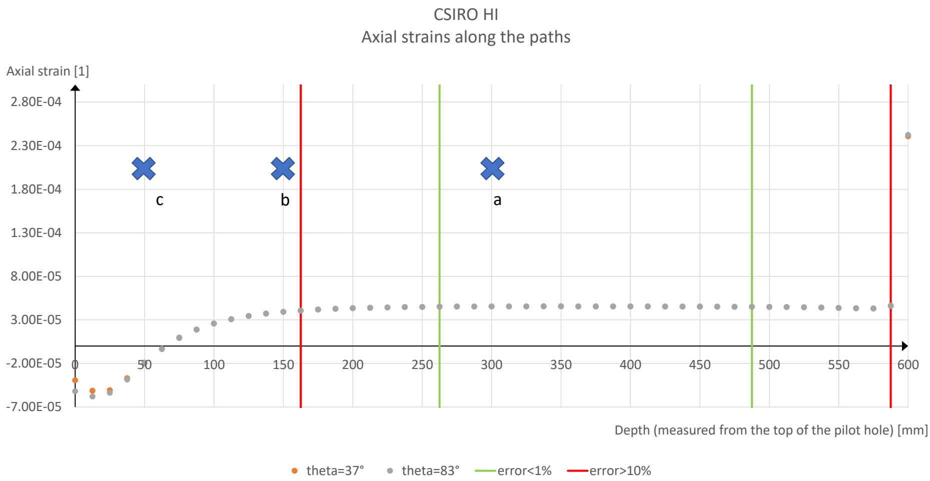

Figure 24. Axial strain ε_z results of the CSIRO simulation in each position. Red and green lines are representing the error correlating to the ε_z result from the middle of the pilot hole. The points marked with a cross are the locations of the simulated measurements.

are used for further calculations. With these input parameters, correction factors can be calculated according to [11]:

$$K_1 = K_2 = K_3 = K_4 = 1. \tag{4.14}$$

This means that the stiffness of the CSIRO HI cell has not been taken into consideration in the model. The fact that the strains are not measured on the pilot hole surface is also neglected.

Firstly, let us substitute strain values shown in Table 11 into equation (3.19), and solve it using (3.22).

Table 11. Tangential strain values from location 'a' (300 mm depth) to be substituted into (3.19). The axial strain at this depth is $\varepsilon_z = 4.54 \cdot 10^{-5}$.

θ [°]	Strain gauge	ε_θ [1]
0	B_{90}	$1.521 \cdot 10^{-4}$
30	E_{90}	$1.675 \cdot 10^{-4}$
60	A_{90}	$1.993 \cdot 10^{-4}$
90	F_{90}	$2.148 \cdot 10^{-4}$

With this evaluation the horizontal components of the in situ stress state can be estimated. These values are presented in Table 12.

Table 12. Comparison of the horizontal in situ stress components calculated from the values in Table 11 and the loads of the model detailed in Subsection 4.2.3

Stress component	Estimation [MPa]	Load [MPa]	Error
σ_x^0	-8.284	-8.21	0.90%
σ_y^0	-7.047	-7.00	0.68%
τ_{xy}^0	-0.001	0	–

The axial normal in situ stress component can be calculated according to (3.23):

$$\sigma_z^0 = \nu_r(\sigma_x^0 + \sigma_y^0) - E_r\varepsilon_z = -7.221\,\mathrm{MPa}. \tag{4.15}$$

It can be seen that the error of the horizontal in situ stress components is less than 1%. As a consequence, the estimation error is minimal if the data is collected from location 'a'. This location is in the interval bounded by the two green lines in Figures 23–24. In terms of σ_z^0, the error value is higher: 3.72%.

The axial (vertical) shear stresses can be calculated according to equations (3.25)–(3.26). Engineering shear strain results can be queried directly from the FE model, therefore the modelling of the diagonal strain gauges is not required. Since the x, y, and z axes of the model coincide with the principal stress directions of the in situ stress state, only normal stress components have been given as boundary conditions. As a consequence, the *in situ* shear stress components derived from the measured strains on the pilot hole surface have to be zero. The queried $\gamma_{\theta z}$ values are negligible compared to the strain results, so the derived τ_{xz}^0 and τ_{yz}^0 are very close to zero.

Let us substitute strain values shown in Table 13 into equation (3.19), and solve it using (3.22). With this evaluation the horizontal components of the in situ stress

Table 13. Tangential strain values from location 'b' (150 mm depth) to be substituted into (3.19). The axial strain at this depth is $\varepsilon_z = 3.917 \cdot 10^{-5}$

θ [°]	Strain gauge	ε_θ [1]
0	B_{90}	$1.589 \cdot 10^{-4}$
30	E_{90}	$1.754 \cdot 10^{-4}$
60	A_{90}	$2.263 \cdot 10^{-4}$
90	F_{90}	$2.225 \cdot 10^{-4}$

state can be estimated. These values are presented in Table 14.

The axial normal in situ stress component can be calculated according to (3.23):

$$\sigma_z^0 = \nu_r(\sigma_x^0 + \sigma_y^0) - E_r\varepsilon_z = -6.913\,\mathrm{MPa}. \tag{4.16}$$

Table 14. Comparison of the horizontal in situ stress components calculated from the values in Table 13 and the loads of the model detailed in Subsection 4.2.3

Stress component	Estimation [MPa]	Load [MPa]	Error
σ_x^0	-8.628	-8.21	5.09%
σ_y^0	-7.299	-7.00	4.29%
τ_{xy}^0	-0.002	0.00	–

It can be seen that the error of the horizontal in situ stress components is around 5%. As a consequence, the error of the estimation increases if the data is collected from location 'b'. This location is in the interval bounded by a green and a red line in Figure 23. In terms of σ_z^0, the error value is higher: 7.83%. Although location 'b' is outside the interval bounded by the two red lines in Figure 24 – so this is not an ideal location to measure axial strains – the estimation of the axial normal stress component is acceptable.

We substitute strain values shown in Table 15 into equation (3.19) and solve it using (3.22).

Table 15. Tangential strain values from location 'c' (50 mm depth) to be substituted into (3.19). The axial strain at this depth is $\varepsilon_z = -1.962 \cdot 10^{-5}$.

θ [°]	Strain gauge	ε_θ [1]
0	B_{90}	$1.817 \cdot 10^{-4}$
30	E_{90}	$2.019 \cdot 10^{-4}$
60	A_{90}	$2.434 \cdot 10^{-4}$
90	F_{90}	$2.638 \cdot 10^{-4}$

The horizontal components of the in situ stress state can be estimated. These values are presented in Table 16.

Table 16. Comparison of the horizontal in situ stress components calculated from the values in Table 15 and the loads of the model detailed in Subsection 4.2.3

Stress component	Estimation [MPa]	Load [MPa]	Error
σ_x^0	-9.374	-8.21	14.18%
σ_y^0	-7.756	-7.00	10.80%
τ_{xy}^0	-0.002	0	–

The axial normal in situ stress component can be calculated according to (3.23):

$$\sigma_z^0 = \nu_r(\sigma_x^0 + \sigma_y^0) - E_r\varepsilon_z = -2.889\,\mathrm{MPa}. \tag{4.17}$$

It can be seen that the error of the horizontal in situ stress components is around 15%. In terms of σ_z^0, the error value is even higher: 61.48%. As a consequence, the estimation is not acceptable if the data is collected from location ‘c’. This location is outside the interval bounded by the two red lines in Figure 23. Based on the results of the simulation, the in situ stress components should not be derived from the data collected by a measurement outside the interval marked with the red lines in Figure 23.

4.2.5. *Summary of CSIRO HI simulation results.* Based on the results of the finite element analysis, the in situ stress components can be estimated from the strains of the pilot hole surface during overcoring as given in Section 3.2. Another conclusion is that the location of the CSIRO HI cell in the pilot hole has a significant effect on the results. The simulation shows that the ideal position of the CSIRO HI cell is between the two green lines in Figure 23, which means a depth between 250–450 mm measured from the top of the pilot hole. Nondimensionalizing the depths by the borehole diameter ($D = 146\,\mathrm{mm}$) produces the following results: in order to make the best approximation, the CSIRO HI cell should be located $1.7D$ beneath the bottom of the borehole, and $1D$ above the bottom of the pilot hole. This agrees with [11], which suggests that the CSIRO HI cell should be located $1.5D - 2.5D$ beneath the bottom of the borehole.

Locating a gauge outside the interval marked by the two red lines in Figure 23 increases the error. In terms of dimensionless values, this means that the HI cell must be located at least $0.7D$ beneath the bottom of the borehole, and at least $0.1D$ above the bottom of the pilot hole in order to obtain an acceptable estimation.

In order to give an accurate estimation for the axial normal in situ stress component σ_z^0, the CSIRO HI cell is recommended to be located in the interval bounded by the two green lines in Figure 24. In terms of depths, this means 262.5–487.5 mm. Nondimensionalizing the depths by the borehole diameter ($D = 146\,\mathrm{mm}$) produces the following results: in order to make the best approximation, the CSIRO HI cell should be located $1.8D$ beneath the bottom of the borehole, and $0.8D$ above the bottom of the pilot hole. If the axial strain values are measured outside the interval bounded by the two red lines in Figure 24, the estimation for σ_z^0 is less reliable. However, as has been demonstrated by the results of location ‘b’, the accuracy of the estimated in situ stress components depends on the tangential strains rather than on the axial strains.

Note that at every location of evaluation, the error of the estimated value of σ_z^0 is greater than the error of the horizontal in situ stress components. The reason for this is that the pressure boundary condition in z direction is applied on the upper horizontal face of the rock mass. This upper face is smaller than the lower face due to the presence of the borehole. The σ_z stress value caused by the reaction force on this lower face – which cannot move in direction z – is $-7.153\,\mathrm{MPa}$.

Furthermore, we can conclude that the assumption made in Subsection 3.2.1 regarding the stress state of the pilot hole at the end of the overcoring is correct based on the results of the simulation (see Figure 25).

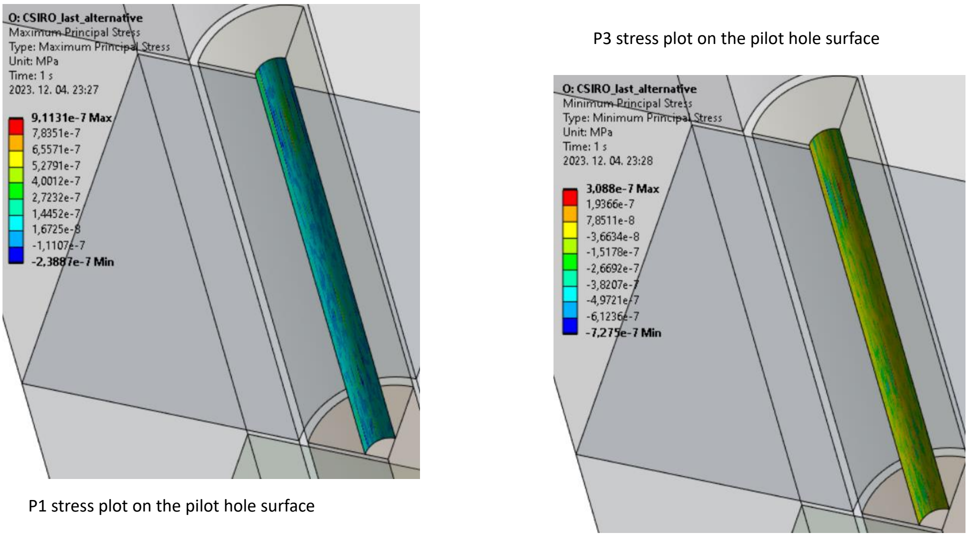

Figure 25. P1 and P3 stress results from Step 3 of the CSIRO simulation. The minimal and maximal values imply that the pilot hole is relieved in this step.

4.2.6. *Plausibility check.* In order to prove the results of the FE model plausible, the force equilibrium has been checked. The vector of the loading forces:

$$\mathbf{F_t} = \begin{bmatrix} p_x A_x \\ p_y A_y \\ p_z A_z \end{bmatrix} = \begin{bmatrix} -5\ 911\ 200 \\ -5\ 040\ 000 \\ -643\ 770 \end{bmatrix} \text{ N.} \tag{4.18}$$

In these equations, A_x, A_y and A_z are the surfaces on which the pressure boundary conditions were defined. The vector of the reaction forces computed from the FEM:

$$\mathbf{F_r} = \begin{bmatrix} 5\ 911\ 200 \\ 5\ 040\ 000 \\ 643\ 610 \end{bmatrix} \text{ N.} \tag{4.19}$$

The sum of the loading and the reaction forces:

$$\mathbf{F_t} + \mathbf{F_r} = \begin{bmatrix} 0 \\ 0 \\ -160 \end{bmatrix} \text{ N.} \tag{4.20}$$

This sum has to be zero. Since $-160\,\text{N}$ is negligible compared to the applied boundary conditions, it can be stated that the reaction forces and the defined loads are in equilibrium.

Besides the reaction forces, the stress field on the borehole surface was also checked. At points which can move along the x direction, σ_x has to be zero. Also at points

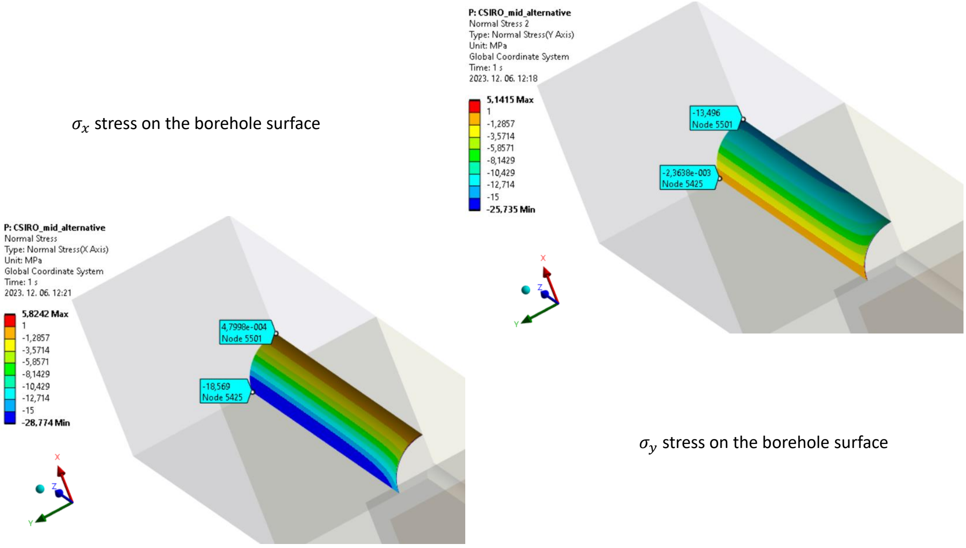

Figure 26. σ_x and σ_y stresses on the borehole surface in Step 2 of the CSIRO HI simulation.

which can move along the y direction, σ_y has to be zero. As shown in Figure 26, the results of the FE model meet these two criteria.

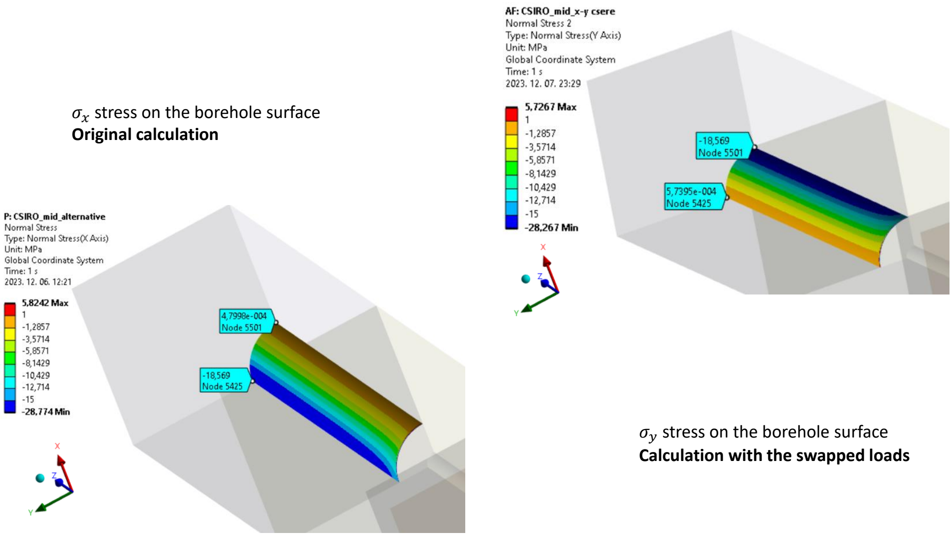

Figure 27. σ_x (left) results of the original simulation, and σ_y (right) results of the simulation carried out with the commuted loads

Furthermore, an analysis with p_x and p_y values commuted was carried out and the stress state of the borehole surface was investigated. The commutation of the loads also commutes the x and y axes. This means the σ_x results of the original computation must be the same as the σ_y results of this new simulation. Based on Figure 27, the results of the FE model meet this criterion. Naturally, the results must be mirrored to the plane defined by the z axis and the $x = y$ line.

The plausibility checks were performed based on the results of Step 2 of the CSIRO HI simulation, since these results are used to derive the in situ stress state. Based on the performed plausibility checks, the results of the FE model are deemed to be plausible.

5. Comparison of the IST and CSIRO HI techniques

In this section, the main conclusions of Section 4 have been collected.

Firstly, based on the results of the finite element analysis, both the IST gauge and CSIRO HI cell can provide enough data to give a correct estimation for the in situ stress state. The detailed evaluation process has been presented in Section 3. According to Table 3, the horizontal in situ stress components can be derived from the deformations measured by the IST gauge with an error less than 1%. According to Table 12, the horizontal in situ stress components can be derived from the strains measured by the CSIRO HI cell with an error of less than 1%. Compared to the IST gauge, the error of the estimation based on the data provided by the CSIRO HI cell is higher. However, the CSIRO HI cell provides enough data to estimate the axial in situ stress components as well. The error of this estimation is less than 5%. Meanwhile, the axial in situ stress components cannot be derived from the data collected by the IST gauge in a single borehole.

It must be emphasized that during the calculations, several assumptions have been made, for example:

- the the rock was considered to be linearly elastic, homogeneous and isotropic,
- the stress state was considered to be identical in any plane perpendicular to the axis of the borehole.

Besides the items mentioned above further assumptions have been made. These are detailed in Subsections 3.1.1 and 3.2.1. We must emphasize that the results of a real measurement can only be less accurate than when calculated by an idealized model, and the robustness of the presently investigated methods in the case of non-ideal circumstances should be assessed to supplement the analysis presented here.

Secondly, based on the results of the finite element analysis, the ideal position of the IST gauge and the CSIRO HI cell has been determined. In order to make the results comparable, the distances have been nondimensionalized by the borehole diameters. This value is $D = 96\,\mathrm{mm}$ in terms of the IST gauge, and $D = 146\,\mathrm{mm}$ in terms of the CSIRO HI cell. The ideal position of the tools is the following:

- the minimal distance between the top of the pilot hole and the IST gauge is $2.1D$,

- the minimal distance between the top of the pilot hole and the CSIRO HI cell is $1.7D$,
- the minimal distance between the bottom of the pilot hole and the IST gauge is $0.8D$,
- the minimal distance between the bottom of the pilot hole and the CSIRO HI cell is $1D$.

Comparing the dimensionless values, it can be stated that the CSIRO HI cell can be located closer to the top of the pilot hole than the IST gauge. However, the IST gauge can be located closer to the pilot hole bottom than the CSIRO HI cell. These optimal intervals are marked by green lines in Figures 28– 29.

To obtain acceptable estimations for the in situ stress components, both the IST gauge and the CSIRO HI cell should be set at least $0.7D$ beneath the top of the pilot hole, and $0.1D$ above the bottom of the pilot hole. This interval is marked by red lines in Figures 28– 29. Note that the optimal location of the CSIRO HI cell has been determined based on the tangential strain results, since the accuracy of the estimations depends more on the tangential strains than the axial strains.

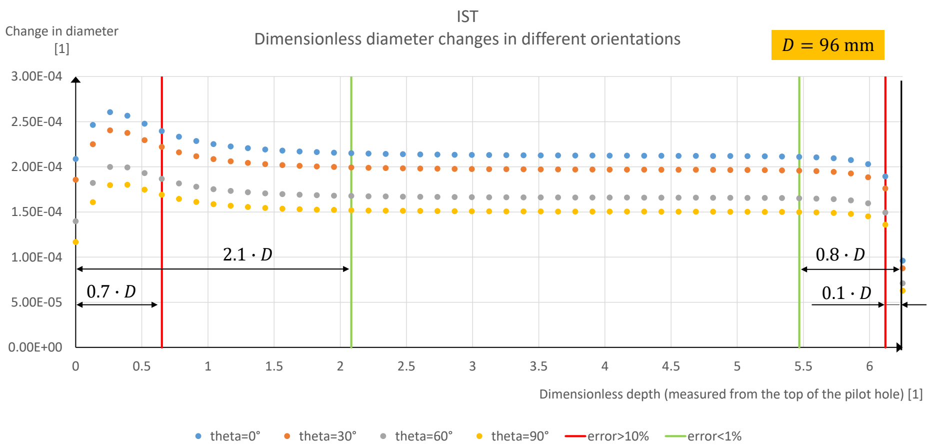

Figure 28. Dimensionless diameter change results of the IST simulation as a function of dimensionless depth in each orientation. The change in diameter values is nondimensionalized by the pilot hole diameter ($d = 25.5$ mm), the depth values by the borehole diameter ($D = 96$ mm).

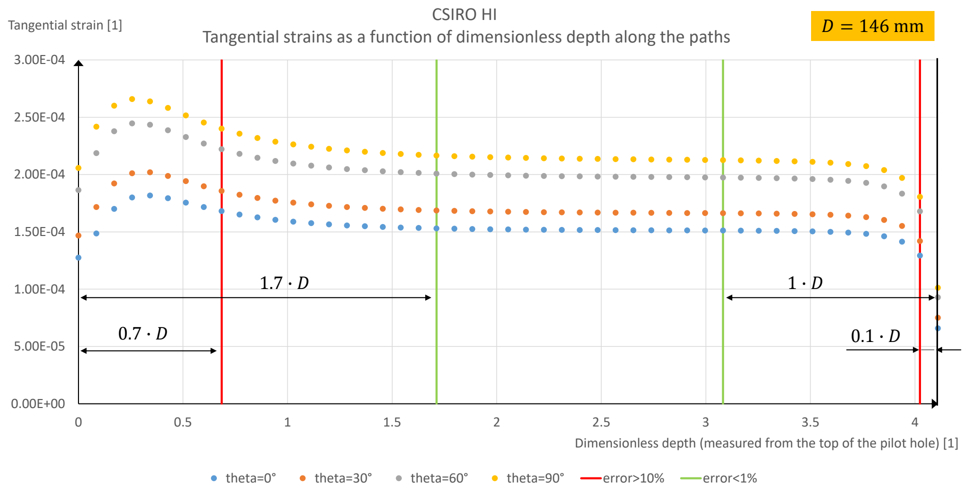

Figure 29. Tangential strain results of the CSIRO HI simulation as a function of dimensionless depth in each position. The depth values are nondimensionalized by the borehole diameter ($D = 146\,\text{mm}$).

6. Discussion

The present work has been carried out with the explicit assumption of homogeneous, isotropic and linearly elastic materials, in accordance with the assumptions made during the derivation of the measurement evaluation methods. However, these assumptions are all based on the necessity of making calculations feasible, while rocks are often non-homogeneous and frequently behave in an anisotropic, viscoelastic way. Thus, relaxing any of these three assumptions during the simulations would yield further valuable insight into the accuracy of the measurement techniques and evaluation methods.

A first step in this direction would be the investigation of the effects of anisotropy on the optimal placement of the instruments used. The size of the optimal and acceptable ranges of placement would, presumably, change significantly even if the condition of isotropy is relaxed to transverse isotropy. Experience of such effects is often considered when overcoring measurements are performed by experts.

Additionally, the effects of the measurement time compared to the relaxation time of a viscoelastically behaving rock type could also influence the accuracy of the estimated in situ stress state. Practical experience as well as analytical calculations [17] suggest that the measurement time indeed influences the displacements and strains observed in a borehole surrounded by a rock mass exhibiting viscoelasticity.

Author contributions

D. Borza: Methodology, Formal analysis, Investigation, Validation, Visualization, Writing – Original Draft. **D.M. Takács:** Conceptualization, Methodology, Supervision, Writing – Review & Editing.

Acknowledgement. We are grateful to László Kovács for his insightful comments regarding the simulations, as well as his kind help in providing some of the technical parameters of the measurement methods. We also thank Tamás Fülöp for drawing our attention to some possible theoretical limitations of the investigated methods.

References

1. Stephansson, O., and Zang, A. "ISRM suggested methods for rock stress estimation – Part 5: establishing a model for the in situ stress at a given site." *The ISRM Suggested Methods for Rock Characterization, Testing and Monitoring: 2007-2014*. Springer, 2014, pp. 187–201.
2. Huasheng, L., Oh, J., Masoumi, H., Canbulat, I., Zhang, C., and Dou, L. "A review of in situ stress measurement techniques." *Proceedings of the 2018 Coal Operators' Conference, Mining Engineering, University of Wollongong, 18-20 February.* 2019.
3. Ljunggren, C., Yanting, C., Janson, T., and Christiansson, R. "An overview of rock stress measurement methods." *International Journal of Rock Mechanics and Mining Sciences,* **40**(7), (2003). Special Issue of the IJRMMS: Rock Stress Estimation ISRM Suggested Methods and Associated Supporting Papers, pp. 975–989. doi: `https://doi.org/10.1016/j.ijrmms.2003.07.003`.
4. Jaeger, J. C., Cook, N. G. W., and Zimmerman, R. *Fundamentals of Rock Mechanics.* Wiley, 2007.
5. Matsuki, K. "An elastic strain recovery compliance of rocks and its application to in situ stress measurement." *International Journal of Rock Mechanics and Mining Sciences,* **45**(6), (2008), pp. 952–956. doi: `10.1016/j.ijrmms.2007.10.005`.
6. Lin, W., Yamamoto, Y., and Hirose, T. "Three-dimensional stress state above and below the plate boundary fault after the 2011 Mw 9.0 Tohoku earthquake." *Earth and Planetary Science Letters,* **601**, (2023), p. 117888.
7. Giot, R., Giraud, A., and Homand, F. "Three-dimensional finite element modelling of stress relaxation tests in anisotropic clayey medium: Direct problem and back analysis." *Geotechnical and Geological Engineering,* 24 (Aug. 2006), pp. 919–947. doi: `10.1007/s10706-005-7723-x`.
8. ASTM. *Standard Test Method for Determination of In Situ Stress in Rock Mass by Overcoring Method – USBM Borehole Deformation Gauge, D4623-08.* Tech. rep. 2008.
9. Gray, I. "The measurement and interpretation of in-situ stress using an overcoring technique from surface." *Proceedings of the 1st Canada-US Rock Mechanics Symposium - Rock Mechanics Meeting Society's Challenges and Demands* **1**, (May 2007), pp. 721–727. doi: `10.1201/NOE0415444019-c89`.

10. LEEMAN, E. R. "The borehole deformation type of rock stress measuring instrument." *International Journal of Rock Mechanics and Mining Sciences & Geomechanics Abstracts,* **4**(1), (1967), pp. 23–44. DOI: https://doi.org/10.1016/0148-9062(67)90003-4.
11. WOROTNICKI, G. "13 - CSIRO Triaxial Stress Measurement Cell." *Rock Testing and Site Characterization.* Ed. by HUDSON, J. A. Oxford: Pergamon, 1993, pp. 329–394. DOI: https://doi.org/10.1016/B978-0-08-042066-0.50020-3.
12. WESTWICK, D. T. and KEARNEY, R. E. *Identification of Nonlinear Physiological Systems.* IEEE Press Series on Biomedical Engineering. Wiley, 2003. DOI: 10.1002/0471722960.
13. BAHRANI, N. and VALLEY, B. "Stress Measurement: The GRC Perspective." World Mining Congress, Montreal, Jan. 2013.
14. KOVÁCS, L. *Jelentés a Bkf-(6-11) jelű fúrásokban elvégzett CSIRO HI-cellás 3D-s és Doorstopper-cellás 2D-s szekunder kőzetfeszültség-meghatározásokról.* Tech. rep. RHK Kft. Adattár: RHK-K-036/16. Pécs: Kőmérő Kft., RHK Kft., June 2016.
15. KOVÁCS, L. and VÁSÁRHELYI, B. "Special requirements for geotechnical characterization of host rocks and designing of a radioactive waste repository." *Engineering Geology for Society and Territory-Volume 6: Applied Geology for Major Engineering Projects.* Springer. 2015, pp. 909–913.
16. PHAM, J., SMITH, D., and GRAY, I. *In situ stress testing on borehole Baf-3 (318 to 835 m depth).* Tech. rep. Sigra Job Reference Number: 511. SIGRA PTY Ltd., Mar. 2021.
17. FÜLÖP, T. and SZÜCS, M. "Analytical solutions for rheological processes around bores and tunnels." *Journal of Engineering Mathematics,* **136**(1) (2022), pp. 1–28. DOI: 10.1007/s10665-022-10235-6.